6

Crosslinked PMMA as a Low-Dimensional Dielectric Sacrificial Layer for MEMS/NEMS and Quantum Nanostructures Fabrication

W.H. Teh[1], J.K. Luo[2], C.-T. Liang[3] and C.G. Smith[4]

[1]*Semiconductor Physics Group, Cavendish Laboratory, University of Cambridge, Madingley Road, Cambridge CB3 0HE, United Kingdom*
[2]*Department of Engineering, University of Cambridge, Trumpington Street, Cambridge CB2 1PZ, United Kingdom*
[3]*Department of Physics, National Taiwan University, Taipei 106, Taiwan*
[4]*Semiconductor Physics Group, Cavendish Laboratory, University of Cambridge, Madingley Road, Cambridge CB3 0HE, United Kingdom and Cavendish Kinetics Ltd., Hugo de Grootlaan 35, 's-Hertogenbosch, 5223 LB, The Netherlands*

1. INTRODUCTION

Microelectromechanical systems (MEMS) is a term that describes the integration of miniaturized mechanical elements with microelectronics through microfabrication technology, so that a mechanical function is coupled with an electrical signal. Nanoelectromechanical systems (NEMS) are MEMS scaled to submicrometer dimensions, to exploit the mechanical degree of freedom on the nanometer scale. In this size regime, it is possible to attain extremely high fundamental frequencies while simultaneously preserving high mechanical responsivity. This combination of attributes translates directly into high force sensitivity, operability at ultra-low power, and the ability to induce non-linearity with very modest

control forces [1], leading to potential payoffs in a diverse range of fields, from medicine to biotechnology to the foundations of quantum mechanics [2, 3]. In order to fabricate MEMS/NEMS devices, the addition, subtraction, modification, and patterning of materials are typically done using techniques originally developed for the integrated circuit (IC) industry, which include lithography, well-controlled etching and precision material deposition.

The two most general methods of MEMS/NEMS fabrication are the bulk and surface micromachining techniques. The discovery of anisotropic silicon etching in the 1960s was an important milestone for the development of bulk micromachining, which is instrumental in the fabrication of the first generation of MEMS. Classic papers describing these crystal-plane-dependent etches are Bean [4] and Bassous [5]. This was later on, complimented by surface micromachining, which provides more flexibility in microfabrication, since shapes are not restricted by the crystallography of the substrate. While the main principle of bulk micromachining is to selectively remove material from a substrate (which is typically, single-crystal silicon) by various etching methods (such as wet isotropic/anisotropic etching, plasma isotropic etching, reactive ion etching and etch-stop techniques), surface micromachining however, uses the principle of depositing, patterning and etching a sequence of thin films. In surface micromachining, an important processing step, which involves the selective removal of an underlying film known as the sacrificial layer, is needed. This sacrificial layer is etched in the final step to undercut the layers above, referred to as the structural layer, so that freestanding movable structures can be formed. The first example of a surface micromachined electromechanical application consisted of an underetched metal cantilever beam for a resonant gate transistor application in 1965 [6]. Although there is no crystallography to depend on for better critical dimension (CD) control, the smaller dimensions of surface-micromachined structures and its straightforward integration with IC components make surface micromachining one of the most commonly used MEMS/NEMS fabrication technologies today. The ability to surface micromachine more complex structures than what is possible in bulk micromachining has been exploited to produce a variety of devices for many different applications.

In surface micromachining, the use of sacrificial layers in between mechanical layers (or structural layers) is necessary for the freedom in movement to be achieved once the mechanical component is released by means of a selective etching step. A surface micromachining process may comprise more than one mechanical layer and more than one sacrificial layer depending on the complexity of the final design. Nevertheless, in principal, surface micromachining requires a well-matched set of mechanical/sacrificial material and release etchant systems: structural materials with the desired mechanical (i.e. minimal residual strain, high yield and fracture strength, minimal creep and fatigue, and good friction-resistance) and chemical properties (i.e. displaying a high-level of inertness to subsequent processing steps), sacrificial materials that allow good adhesion, low pin-holes density and low residual stress, and release etchant systems (both chemical and physical) that have excellent etch selectivity with respect to the sacrificial material and also, appropriate viscosity and surface tension characteristics [7].

Many different types of sacrificial layers have been used, which include metallic and non-metallic layers. One of the earliest examples of surface micromachining involves the polysilicon/oxide material system where free-standing LPCVD polysilicon structures were realized by removing the oxide layers that reside below [8, 9]. Other variants of non-metallic sacrificial layers include: the silicon nitride/polysilicon material system where silicon nitride is used as the structural material and poly-Si as the sacrificial material, and

the tungsten/silicon dioxide material system where CVD tungsten is used as the mechanical layer with the oxide as the sacrificial layer. An early review of the surface micromachining technology with an emphasis on polysilicon microstructures is given by Howe [10]. In a separate material system, metallic sacrificial layers were used, such as the polyimide/aluminum material system where polyimide surface microstructures were made by selectively etching an aluminum sacrificial layer [11]. Metallic sacrificial layers such as copper, aluminum, titanium and chromium have also been used [12–16] extensively for most MEMS developed using LIGA-like processes.

There are several disadvantages in using these common sacrificial layers. For the release mechanism, wet etching is typically used, where in the final step, the wafers are usually rinsed in deionised (DI) water and dried. Without properly designed microstructures (i.e. by having thicker structural and sacrificial layers or by placing deflection bumps at the bottom of the contacting layers), the wet etch release process may result in the permanent adhesion of the suspended microstructures. This is caused by the large capillary and surface tension forces of liquids, which induce stiction, rendering the devices to fail. As for on-chip integration, the release step often involves aggressive etchants (i.e. HF solution to remove sacrificial oxide and KOH solution for etching polysilicon) making compatibility with conventional IC processing difficult. As an example, the aggressive etchants may attack the passivating oxide or the aluminum metallization. In most cases, these aggressive wet etchants cannot be avoided as a result of the strict requirement in terms of etch selectivity between the structural and sacrificial layer, especially when we scale down into smaller and smaller dimensions. This limitation is worsened when one uses bulk micromachining techniques where crystal orientation and geometrical shapes are also important considerations. Also, due to the importance placed in the residual stress of the structural layers, inertness at the interface between the structural and sacrificial layers has to be ensured (with processing temperatures considered) to avoid possible diffusion of ions and atomic species. This is because uncontrolled reaction between the structural and sacrificial layer may result in unwanted stress, which causes buckling [17, 18]. Additionally, coating of typical sacrificial layer materials based on thermal evaporation or sputtering techniques is costly and time-consuming, and is thus, not suitable to make show and tell parts for prototyping purposes. These sacrificial materials cannot be dissolved easily and cannot be patterned directly and in most cases, require an additional mask step, making them less cost-effective. All the above disadvantages regarding existing sacrificial layer materials may restrict advances in using new thin film materials as the structural layer. The need to experiment with more exotic structural materials may be a fundamental necessity to meet wear and abrasion requirements as well as enable certain transduction characteristics of MEMS/NEMS.

Consequently, new sacrificial materials such as organic-based or polymeric materials have been introduced to circumvent most of the problems faced by conventional sacrificial materials (i.e. silicon dioxide, phospho-silicate glass, polycrystalline silicon, and etc.). Organic-based sacrificial materials such as photoresist [19, 20] and polyimide [21] have been primarily used to offer an excellent etch selectivity so that the structural material choice can be extended to include more exotic ones such as SiC, SiN and Ti [21]. In addition, the combination of an organic-based sacrificial material with a dry-release step in oxygen plasma helps to eliminate stiction problems and simplifies processing as compared to wet-etching release. The oxygen plasma dry release technique is also fully compatible with conventional silicon IC processing and this compatibility can be achieved by means of a post-processing approach. Typical organic-based sacrificial layer materials are easy to coat,

low-cost, easy to dissolve, can be patterned directly and is compatible with most materials and processes used in conventional IC processing. A good example of a commercial product based on organic sacrificial materials is the Texas Instruments Digital Mirror Device, which is created using aluminum as the structural material, and photoresist as the sacrificial material [22]. Recently, dendritic materials such as hyperbranched polymer HB560 [23] has also been reported as a high etch rate dry-release sacrificial layer allowing large-area and high aspect ratio release. For these organic-based sacrificial materials, they are patterned either directly or indirectly by optical lithography and is thus, limited to critical sizes which are usually in the same order of magnitude as the structural layers, which is in the tens to hundreds of micrometers range. In other words, in spite of the flexibility provided by these reported organic-based sacrificial materials (i.e. photoresist, and etc.), advanced lithographic approaches such as electron beam lithography (EBL) is not exploited to further miniaturize the structural/sacrificial layers to bring us to the regime of NEMS. This clearly becomes a limiting factor in fabricating NEMS devices, which may provide a revolution in basic and applied research.

The intent of this chapter is therefore, to introduce a surface nanomachining process that will be interesting to NEMS researchers because not only does it has the merits of the organic-based sacrificial materials discussed above, but this process also employ EBL for the patterning of both the structural and sacrificial layers. This surface nanomachining process, which is based on crosslinked polymethyl methacrylate (PMMA) as the low-dimensional dielectric sacrificial layer, uses an oxygen plasma dry release step, is fully compatible with conventional silicon IC processing and eliminates stiction problems. More importantly, the use of EBL allows the further miniaturization of MEMS into the NEMS domain and the fact that the mechanical and sacrificial layers can be patterned in the same step, help to provide flexibility and quick turn-around time in the processing of NEMS devices. This chapter begins by reporting on the characterization of crosslinked PMMA electron beam resist. This is then followed by the development of the crosslinked PMMA surface nanomachining process to fabricate basic MEMS/NEMS components. Based on dose modulation, this technique, which uses EBL, offers high-resolution quasi 3-D nanomachining of the sacrificial layer in a single run with the advantage of producing low-stress mechanical structures that will be suitable for both applications and fundamental research. For the former, reported examples include: the fabrication and electrostatic actuation of one of the smallest near-zero curvature Ni micromechanical tunneling switch, the development of a simple and innovative methodology to enable the integration of high yield, uniform and preferential growth of vertically-aligned carbon nanotubes on low stress micro/nanomechanical structures and finally, the development and characterization of fabricated thermal microactuators. As for the purpose of fundamental research at low temperatures (i.e. down to 50 mK), crosslinked PMMA as an excellent gate dielectric is demonstrated by the fabrication of multilayered gated quantum devices.

2. CROSSLINKED PMMA AS A LOW-DIMENSIONAL DIELECTRIC SACRIFICIAL LAYER

In this section of the chapter, we report the development and the characterization of a novel, simple and flexible surface nanomachining process using electron beam crosslinked

PMMA as an alternative to fabricate MEMS/NEMS devices. PMMA with different molecular weights (i.e. MW 100K, MW 495K, MW 950K), dissolved in anisole casting solvent has been crosslinked with different electron beam irradiation levels ranging from 20 C/m^2 to 240 C/m^2 to investigate the quantifiable relationship between electron dose and its submicrometer remaining thickness after dissolution in acetone. The results derived from this relationship facilitate the development of a high-resolution quasi 3-D nanomachining capability of the sacrificial layer in the same EBL step based on dose modulation. As a result, this avoids the need to pile up two-dimensional layers one after another for the same purpose. Since crosslinked PMMA has a relatively low value of Young's modulus of about 4–5 GPa, it offers a high degree of compliance and thus, has the advantage of producing low-stress submicrometer thick structures with lateral dimensions as low as, but not limited to 1 μm. The high compliance of crosslinked PMMA allows the stress relaxation of the mechanical structures to begin after the deposition of each mechanical layer. This happens prior to the stiction-free dry release step. A fast dry release time of 55–100 s using oxygen plasma ashing has been demonstrated for a sacrificial layer aspect ratio of 125 (which is given by the lateral undercutting divided by the thickness of the layer). This corresponds to an etch rate of about 0.6 μm/s at an average temperature of 40°C. This surface nanomachining process is capable of producing submicrometer gaps as low as, but not limited to 30 nm high.

2.1. PMMA Resist for Electron Beam Nanolithography

Standard lithographic approaches use UV light to expose a resist layer. However, in most cases, diffraction imposes a limit on the resolution of the patterning process. In contrast, EBL, which is based on the direct writing of patterns using electron beams with energies in the keV range, is not limited by diffraction. In this technique, the energy imparted by the well-controlled stream of electrons modifies the chemical characteristics of the resist layer that was spun on the surface of a substrate prior to the exposure. The chemically modified resist is then selectively dissolved in a suitable developer to create a template. This polymer-based template is subsequently used for etching or another form of transfer (such as the lift-off process) of the desired pattern into the substrate. The EBL approach is flexible to be scanned in any desired two-dimensional patterns without the need for the fabrication of conventional mask-plates. Due to the similarity in the fundamental reliance of EBL and scanning electron microscopy (SEM) on directing narrow electron beams, it is therefore common for researchers to modify SEMs into basic EBL systems. Here, the position of the electron beam is controlled, and in conjunction with a beam blanker that modulates the beam current, can enable high resolution patterning [24]. Due to its direct writing mode, EBL has difficulty in throughput (and hence, is not used in conventional IC manufacturing processes) as compared to other technologies such as optical projection lithography. In spite of this difficulty, EBL has been exploited to miniaturize MEMS into the regime of NEMS, which may provide a revolution in applications such as sensors, photonics, biomedical diagnostics, display systems and data storage as well as enabling physics-motivated research in low-dimensional systems. For a further discussion on EBL, see for example, ref. [25].

PMMA positive resists are based on special grades of poly (methyl methacrylate) designed to provide high contrast and high resolution for EBL, deep UV (220–250 nm) and X-ray lithographic processes. Also, PMMA is often used as a protective film in

III–V device wafer thinning applications. PMMA is probably the highest resolution organic photoresist used for EBL with the intrinsic limit in PMMA generally thought to be about 10 nm although recent work has suggested that lines as small as 6 nm are also possible [26]. The ultimate resolution achievable in a resist is determined by many factors: the properties of the resist, the properties of the exposing beam, beam-resist interactions, effects of the developer and development conditions (such as ultrasonic agitation), and the pattern transfer to the substrate. In general, higher resolution is achieved through the use of narrow and bright beams, higher contrast developers, ultrasonic agitation, and the use of high polymer molecular weights. However, it should be noted that in most cases, the beam diameter is not the limiting factor for the resolution of a given resist system but rather the interactions between the electrons and the solid. These interactions result in forward and backscattered electrons, and also, low energy secondary electrons, all of which contribute to the exposure. The proposed use of membrane substrates to reduce backscattered electron contribution to the exposure has been found not to improve the ultimate resolution but may improve the exposure dose latitude [26]. This is due to the low energy secondary electron contribution from the interaction with the resist. When an electron beam impinges on a resist layer, the electrons scatter through both elastic and inelastic processes. The former process leads to the backscattering of the electrons at energies close to the primary beam and innegligible energy transfer to the resist and substrate while the latter process leads to spreading of the primary beam and generation of low-energy secondary electrons that, in turn, expose the resist [24]. In the case of chemically amplified resists (which consists of three components: an acid generator, cross-linker and resin matrix), the diffusion of the acid catalyst during the post-exposure bake makes an additional contribution to the ultimate resolution. Despite much experimental evidence, the mechanisms that determine the ultimate resolution remain vague.

2.2. Crosslinked PMMA Electron Beam Resist

PMMA, being a long chain molecule with a monomer structure shown in fig. 1, is characterized by a reduction of molecular weight owing to chain scission of the original molecule after exposure. Typical unexposed, high-resolution PMMA has a molecular weight

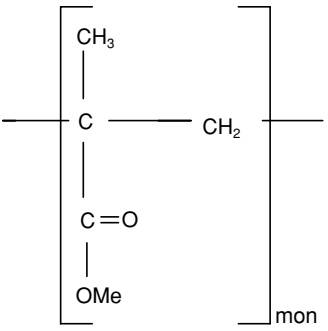

FIGURE 1. Monomer structure of poly(methyl) methacrylate (PMMA) resist. The molecular weights (MW) of PMMA used in this study are MW 100 K, 495 K and 950 K dissolved in an anisole casting solvent.

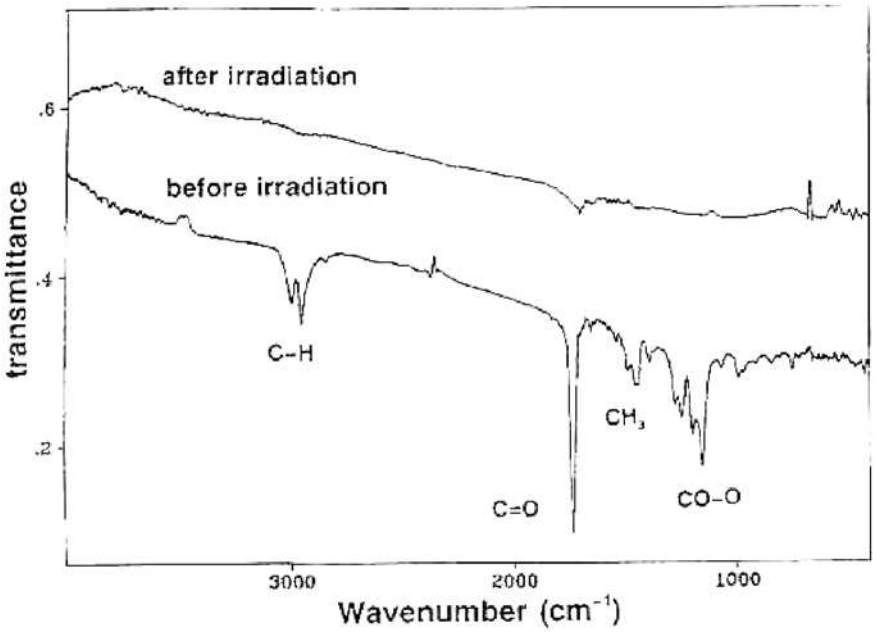

FIGURE 2. Infrared absorption spectra of exposed and unexposed PMMA resist. The dose of the 20 keV electrons is 0.1 C/cm^2. (From T. Tada *et. al.* (1995) *J. Vac. Sci. Technol. B*, **13**, 2801–2804. © 1995 American Institute of Physics. With permission.)

of about 10^6 Da, which is reduced to a few thousand Da after exposure [27]. As a result, this makes the exposed region more sensitive to dissolution in liquid developers such as methyl isobutyl ketone (MIBK) mixed with isopropanol (IPA) in a ratio of 1:3 or 2-ethoxyethanol (Cellosolve) mixed with MeOH in a ratio of 3:7. This makes PMMA a positive resist for conventional EBL applications.

However, this behavior does not extend to infinite dose and at higher exposure doses, crosslinking events dominate and the resist becomes less soluble [28]. In other words, PMMA will crosslink to act as a negative resist. Fig. 2 shows infrared absorption spectra of PMMA (with an average MW of 6×10^5 amu) on silicon substrates before and after a high dose EBL exposure (0.1 C/cm^2) [29]. The infrared spectra demonstrates that the absorption peaks assigned to C-H stretch, C=O stretch, CO-O stretch, and CH_3 bending almost disappears after high dose EBL exposure. This suggests that the side chains of PMMA molecules are detached by high electron beam irradiation levels and the exposed PMMA has a carbon-like composition [29]. Consequently, the PMMA resist is no longer soluble in developing solvents and acts as a negative resist. The resolution of a negative resist is limited by the molecular size of the resist and because the molecular size of PMMA decreases as a result of chain-breaking, implies that the intrinsic resolution as a negative resist is good independent of the initial molecular size [29]. Some of the earlier work on exploiting this crosslinking property is the report on the fabrication of Si pillars with a width of 10 nm and a height of 95 nm based on an electron cyclotron resonance (ECR) etcher [29]. This is performed by carefully developing highly dosed PMMA in acetone to yield features as small

as 10 nm. Here, it was found that as the dose is increased, resistance to dry etching increases to about twice that of unexposed PMMA. EBL crosslinked PMMA has also been employed by Zailer *et. al.* [30] to allow the patterning of submicrometer features in an insulating layer to facilitate experiments in nanostructure physics. Here, the crosslinked PMMA layer serves as a good, uniform insulating layer to fabricate various multilayer devices comprising of conducting and insulating layers. The ability to observe oscillations in both the integer and the fractional quantum Hall regime in a dilution refrigerator demonstrates that the high dose exposure required to crosslinked the PMMA does not degrade the heterojunction transport characteristics appreciably. As for MEMS/NEMS fabrication, it was found [17, 18] that by crosslinking with each other to form a network of larger molecules, crosslinked PMMA becomes resistant to most solvents including acetone, but remains easily etched in oxygen plasma. This property of being a high-resolution negative resist at high electron irradiation levels can be utilized as a unique nanomachining process to pattern the sacrificial layer for MEMS/NEMS fabrication. By using higher exposure doses, the PMMA resist can be selectively crosslinked to various degrees using EBL to define a low-dimensional sacrificial layer with resolutions typically achieved by EBL. In other words, by controlling the localized amount of electron dose that it receives, PMMA can be used as a positive and negative resist in the same fabrication step. This is perhaps one of the simplest ways to fabricate prototype NEMS devices with a quick turn-around time and provides good structural material compatibility since crosslinked PMMA is easily etched in oxygen plasma. We demonstrate this technique by reporting the characterization of PMMA as a function of electron irradiation levels and by referring to fabricated micro/nanomechanical structures and devices.

2.3. Crosslinked PMMA Characterization

In this subsection of the chapter, experiments [17] are carried out so that the quantifiable relationship between electron beam irradiation doses and the remaining thickness of crosslinked PMMA layer (after dissolving in acetone and various developers) can be identified. The dose dependence of the crosslinking process in PMMA resist, important for the development of a sacrificial layer surface nanomachining process, is later on, in the next subsection, used to realize a quasi 3-D technique to fabricate basic MEMS/NEMS components.

For the characterization experiments, neat PMMA with molecular weights (MW) of 100 K, 495 K and 950 K are used, with 6%, 5% and 4% solid content in an anisole casting solvent, respectively. The trend of reducing the solid content as the MW of the PMMA increases is in order to maintain similar spin-on film thickness-spin speed curve across all MW. Characterization of each type of PMMA is performed by first spinning the resist on a Si substrate at 6000 rpm (50 s) in two steps, with the first layer baked for 7 mins and the second a subsequent 30 mins, both at 150°C. This is important to obtain an overall thicker resist, which can still remain quantifiable even though the given spin-on film thickness-spin speed curve from the supplier has a limited range in terms of spin-on thicknesses. Also, by spinning on multiple thin PMMA layers instead of one thick layer, has the advantage of maintaining reasonable uniformity across the substrate to avoid potential edge beads effects. This is because thinner resist is spun at a much higher spin speed where the gradient of the spin-on film thickness-spin speed curve is considerably low. Before electron beam

exposure, the spun-on bilayer PMMA resist for MW 100 K, 495 K and 950 K are measured to be 2065 Å, 3432 Å and 3264 Å thick, respectively. Thereafter, the bilayer PMMA resist is selectively crosslinked by electron beam at different electron doses (20 C/m^2 to 240 C/m^2) using a modified Hitachi S800 SEM at an accelerating voltage of 25 kV. A Dektak surface profiler is used to measure the resulting difference in the remaining PMMA thickness after the corresponding dissolution steps. These include dissolving the exposed PMMA resist in 3 IPA: 1 MIBK developer for 40 s followed by IPA rinse well as dissolution (if any) in acetone for 7 mins followed by IPA rinse. The results of these experiments are shown in figs. 3 and 4.

Figure 3 shows the influence of electron beam exposure doses on the solubility of PMMA resist in 3 IPA: 1 MIBK developer and acetone for electron doses ranging from 20 C/m^2 to 240 C/m^2. Fig. 3(a)–(c) correspond to the characterization of the bilayer PMMA resist with various fragmented MW of 100 K, 495 K and 950 K with respective initial spin-on thicknesses of 2065 Å, 3432 Å and 3264 Å, as measured by the Dektak surface profiler. From fig. 3, it can be observed that a distinct reduction of the thickness of the bilayer PMMA resist occurs upon electron beam exposure as a function of the dose. This reduction was quantified to be approximately 25% to 50% of the original PMMA thickness whereby a higher reduction of thickness is noticed for higher electron doses. Here, the rate of reduction decreases as a function of dose and plateaus off at around 90 C/m^2, 110 C/m^2 and 120 C/m^2 for PMMA MW 100 K, 495 K and 950 K, respectively. This is most probably due to the evaporation of the volatile anisole casting solvent and can be a function of the pre-exposure baking time. Upon further development in 3 IPA: 1 MIBK developer and acetone, a further reduction in the remaining thickness is noted, especially for irradiation doses which are lower than 100 C/m^2. Depending on the level of electron irradiation (or in other words, the amount of energy the PMMA resist receives), the magnitude of crosslinking events ranges from partial crosslinking to full crosslinking. Moderate dose ($<$30–40 C/m^2) electron irradiation of the PMMA simply degrades the resist and forms fragments of lower MW and hence is totally removed in the developer and acetone (as is the case for conventional EBL where PMMA acts as a positive resist). However, at higher irradiation doses ($\sim$40–100 C/m^2), the PMMA molecules start to crosslink with each other to form a network of larger molecules. Here, the regions near the top of the resist are not crosslinked completely (as the dose received by the regions near the bottom of the resist are exacerbated by backscattered electrons) and hence, are washed away in acetone. Depending on the sensitivity (which depends on the molecular weight) of the PMMA resist used, different doses are needed to initiate full crosslinking. This is consistent with the results shown in fig. 4.

Figure 4 shows an overall comparison of the normalized thickness of the remaining crosslinked PMMA resist after dissolving in acetone for MW 100 K, 495 K and 950 K. The inset of fig. 4 shows the characterization of the same, but with the electron dose extended up to 480 C/m^2 (where the initial spin-on thickness for this particular PMMA MW 495 K sample is about 319 nm). From fig. 4, it is estimated that the electron dose needed to initiate full crosslinking is around 100 C/m^2, 110 C/m^2 and 120 C/m^2 for MW 100 K, 495 K and 950 K, respectively. Also, the minimum amount of electron dose to start the onset of PMMA crosslinking is found to be approximately 40 C/m^2 for both MW 100 K and 495 K, and 60 C/m^2 for the MW 950 K resist. The amount of absorbed energy density, which is in general a complicated function of position within the resist film, will result in the partial dissolution of PMMA in acetone if full crosslinking does not happen across its entire thickness (i.e. for

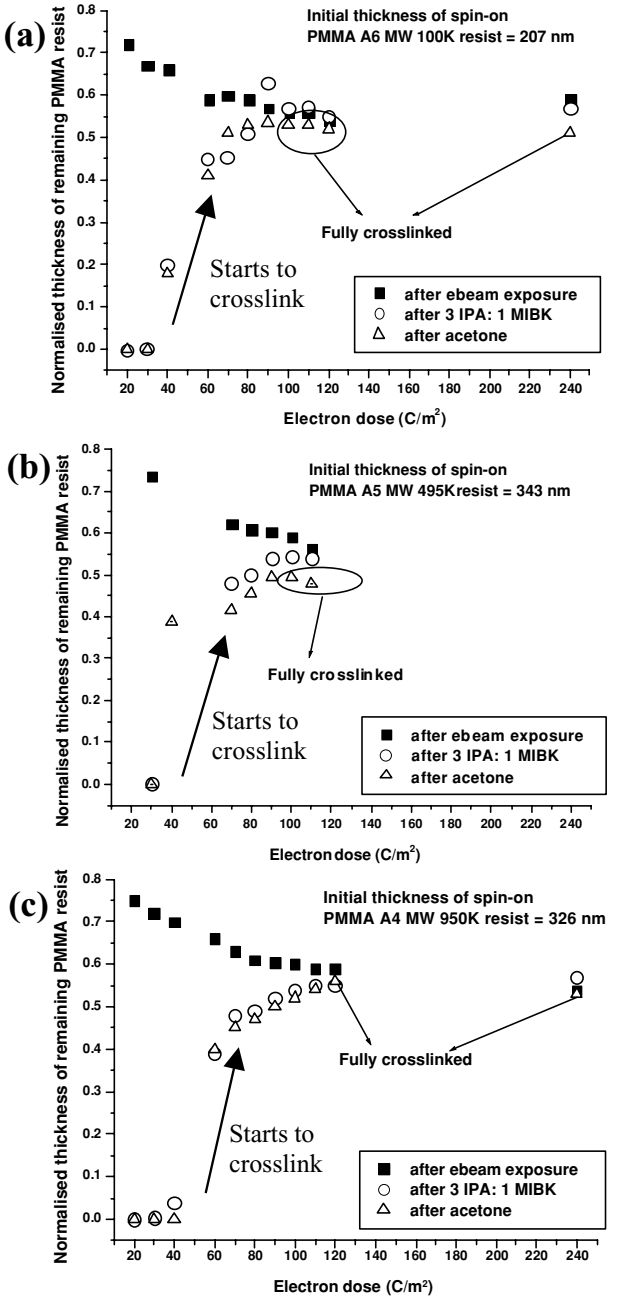

FIGURE 3. Solubility characteristics of electron beam exposed poly(methyl) methacrylate (PMMA) in the form of its remaining thickness normalized to its initial spin-on thickness as a function of electron dose at 25 kV for different development steps for (a) MW 100 K (b) MW 495 K and (c) MW 950 K. (Adapted from W.H. Teh *et. al.* (2003) *IEEE/ASME J. Microelectromech. Syst.*, **12**, 641–648. © 2003 IEEE. With permission.)

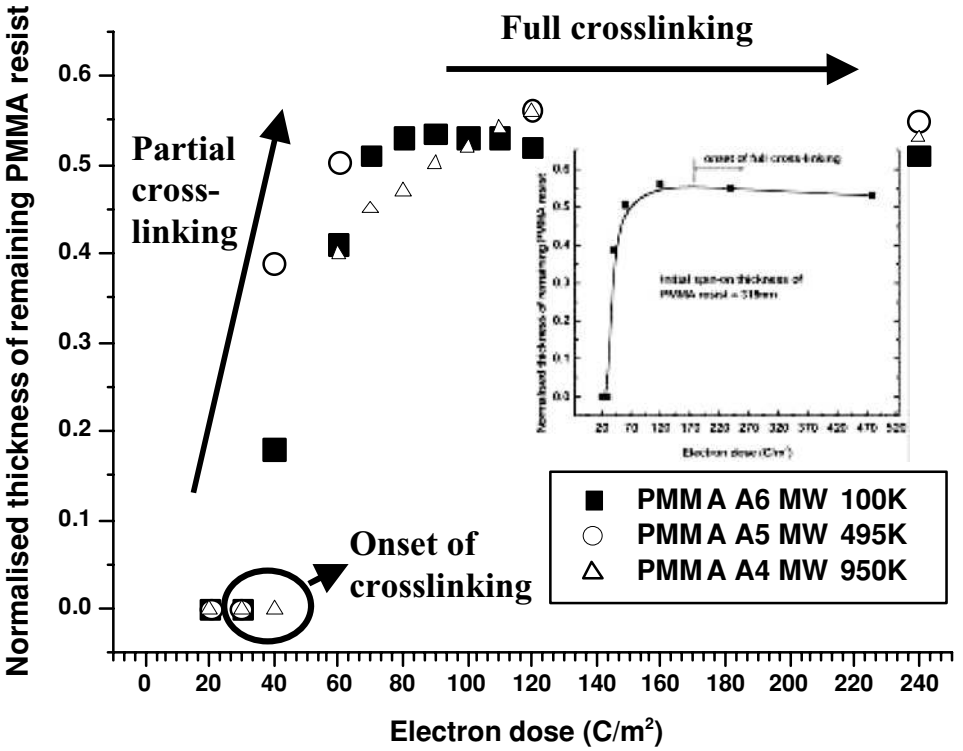

FIGURE 4. A direct comparison of the normalized thickness of the remaining crosslinked PMMA resist after dissolving in acetone for different molecular weights. Inset graph: Characterization of the same with the electron dose extended up to 480 C/m^2. The initial spin-on thickness for this sample (PMMA MW495 K) is about 319 nm. (Adapted from ref. [17])

doses between the onset of crosslinking and full crosslinking). This explains the increase in the remaining thickness of the crosslinked PMMA resist (after dissolving in acetone) as the crosslinking becomes more 'complete'. Other factors that play a role in determining the threshold dose for crosslinking include beam energy, resist thickness, type of substrate, and the geometry of the irradiated pattern [28]. The remaining thickness of the crosslinked PMMA resist increases as a function of dose (when the dose is beyond the crosslinking threshold) until it forms a plateau. The formation of this plateau is an indication that all of the PMMA molecules have been crosslinked. At this point, the effective shrinkage of the resist is near 50% from its initial spin-on value. The large shrinkage of the resist as a result of complete crosslinking has been exploited to produce submicrometer gaps between 30–450 nm. The reduction of the PMMA thickness at full crosslinking is predominantly due to the removal of side chains of the PMMA molecules [29]. In addition, a slight decrease in thickness is observed beyond this, because of the intense agglomeration of the network of crosslinked PMMA molecules and also, low volatility products, which are formed during irradiation, leave the polymer.

An atomic force microscopy (AFM) scan of a crosslinked PMMA sample (MW 495 K) spun on at 3000 rpm for 50 s is performed at a scan size of 40 $\times$ 40 μm^2 and a scan rate of

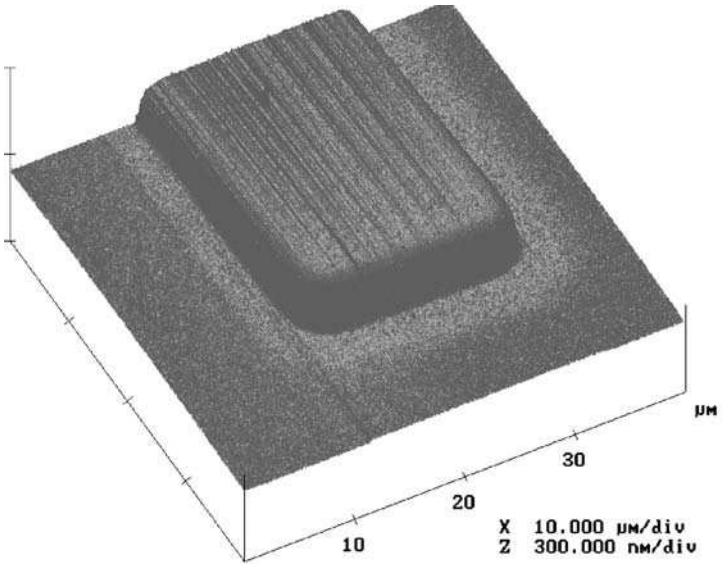

FIGURE 5. An AFM micrograph with a scan size of $40 \times 40\ \mu m^2$ at a scan rate of 0.7 Hz of an EBL crosslinked PMMA (MW 495 K) layer with a dose of 60 C/m^2 at 25 kV.

0.7 Hz. This particular sample is crosslinked using an electron dose of 60 C/m^2 at 25 kV and is AFM scanned to investigate its surface roughness. Fig. 5 shows the results of the AFM scanned EBL crosslinked PMMA (MW 495 K) layer. From fig. 5, an average surface roughness of 2.2 nm can be obtained as compared to a surface roughness of 1.96 nm before crosslinking. The relatively smooth surface of crosslinked PMMA with no observed pin-holes is ideal for the deposition of structural layers on top of it when used as a low-dimensional sacrificial or dielectric layer. Also, as evident from fig. 5, the sidewalls of the crosslinked PMMA layer have a reasonably straight profile due to the nature of electron beam exposure and the high degree of crosslinking incurred.

2.4. Quasi 3-D Fabrication of MEMS and NEMS

For the fabrication of basic MEMS and NEMS suspended components, Ti/SiO_2/Ni multilayers were used as the structural material with electron beam crosslinked PMMA as the low-dimensional sacrificial material [17]. The multilayer material Ti/SiO_2/Ni was chosen for the demonstration of the developed surface nanomachining technique because in the final step, the suspended structures will serve as a platform for growing multi-walled carbon nanotubes on them. Here, the SiO_2 layer serves as the diffusion barrier and the Ni layer is the catalyst layer. Further details on the work concerning the integration of carbon nanotubes with MEMS/NEMS structures will be provided in subsection 3.2.

To pattern the sacrificial layers in a quasi 3-D manner, dose modulation using a single EBL step was used to crosslink the PMMA layer. This technique is schematically shown in fig. 6. Depending on the size of the final gap that separates the mechanical layer and the substrate (and also, taking into account the resulting thickness reduction once selectively crosslinked by electron beam with different irradiation levels), the process starts by spinning single or multiple layers of PMMA (MW 495 K) on a substrate [see fig. 6(a)]. The substrate

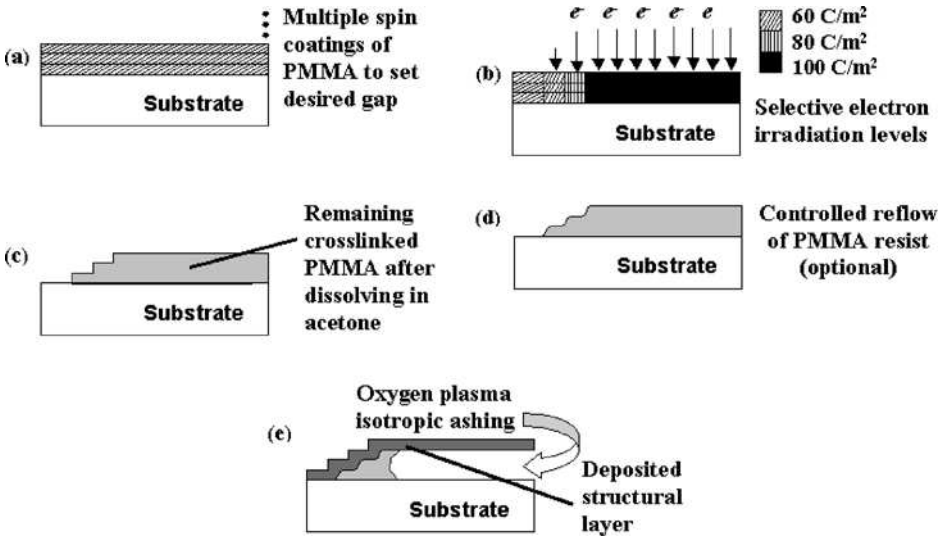

FIGURE 6. A general schematic diagram showing the fabrication process of suspended micromechanical structures using the developed crosslinked PMMA quasi 3-D surface nanomachining technique. An optional reflow step is used to improve the slope of sidewalls. Using this method, multiple shifted exposures of the same pattern for a similar purpose is no longer necessary. (From W.H. Teh *et. al.* (2003) *J. Vac. Sci. Technol. B*, **21**, 3007–3011. © 2003 American Institute of Physics. With permission.)

used for this purpose is (100) antimony doped n^{++} Si (cleaned with hydrofluoric acid) with nominal resistivities measuring between 3–10 Ω cm. These spun-on PMMA layers are pre-baked for about 30–40 mins at 150 °C, followed by localized electron beam irradiation with different doses [see fig. 6(b)] to obtain the desired quasi 3-D patterning effect. The use of different electron irradiation levels in a single exposure to modulate the thickness of the crosslinked PMMA sacrificial layer circumvents the need to pile up two-dimensional layers. To demonstrate the capability of quasi 3-D patterning of the crosslinked PMMA in a single run, multiple steps were made near the edges of the sacrificial layer using electron doses of 60 C/m^2, 80 C/m^2 and 100 C/m^2 [see fig. 6(b)] followed by dissolution in acetone. Acetone dissolution follows to wash away the PMMA regions which are not crosslinked [see fig. 6(c)]. An optional reflow step [see fig. 6(d)] can be used to reduce the slope of sidewalls. This can improve the rigidity of the mechanical structure by avoiding potential high-stress 'spots'. Using this method, multiple shifted exposures of the same pattern [20] to obtain a similar stepping effect at the edge is no longer necessary. The advantage of variable-dose writing with doses that range in between the initiation and the complete crosslinking of the PMMA layers is that these crosslinked sacrificial layers will not be dissolved in the subsequent mechanical layer patterning steps that require lift-off in acetone. In other words, profile writing based on dissolution rate in acetone for PMMA in the negative tone is used. This is different to using the dependence of dissolution rate on dose for PMMA in the positive tone, as described by E. Kley in ref. [31].

As for the structural patterning of NEMS components, which requires better resolution, PMMA is spun on top of the crosslinked PMMA sacrificial layers to enable a standard dose (i.e. 2–9 C/m^2 depending on the dimensions) EBL to be performed. This step can be replaced with standard optical resist if parallel optical lithography is preferred, or when it involves the

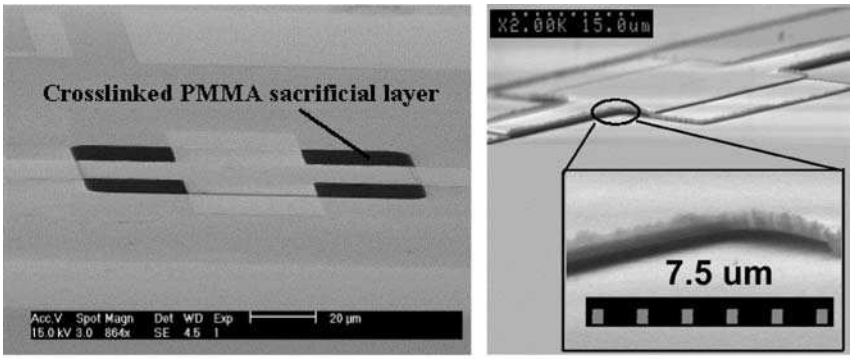

FIGURE 7. SEM micrographs showing (a) a Ti/SiO_2/Ni cross micro-membrane with a visible 160 nm thick crosslinked PMMA sacrificial layer underneath and (b) a fully released Ti/SiO_2/Ni floating cross micromembrane after 55 s isotropic ashing in oxygen plasma. The dry release yields lateral underetching of more than 20 μm per side with an average sacrificial layer aspect ratio of 125. The inset shown is 4× magnified. (From W.H. Teh *et. al.* (2003) *IEEE/ASME J. Microelectromech. Syst.*, **12**, 641–648. © 2003 IEEE. With permission.)

lower-resolution case of MEMS fabrication. Finally, the structural materials were deposited and lifted off in acetone. The structural materials consist of 120–180 nm thick evaporated Ti followed by magnetron sputtered 8 nm thick SiO_2 and 2–4 nm thick sputtered Ni. The final dry release step involves oxygen plasma ashing for 55–150 s (with intermittent breaks of a few mins every 40 s to avoid overheating) using a microwave plasma stripper (Plasmatic Systems, Inc.) with an O_2 gas flow of 100 sccm at a base pressure of about 10^{-1} to 10^{-2} mbar. This provides an isotropic etch rate of about 0.6 μm/s at a nominal power of 1.4 kW [see fig. 6(e)].

Using the developed process, suspended MEMS structures in the form of cross micromembranes are successfully fabricated [17]. Here, optical lithography is used for the patterning of the mechanical structures and EBL for the sacrificial layer. Fig. 7(a) shows an SEM micrograph of the Ti/SiO_2/Ni cross micro-membrane before release. The cross pattern was deposited over a 100 μm × 100 μm crosslinked PMMA sacrificial layer measuring 160 nm in thickness. Dry release of the micromechanical structure, as seen in fig. 7(b) has been achieved using isotropic oxygen plasma ashing. The inset of fig. 7(b) is 4 × magnified to reveal successful underetching of more than 20 μm per side with an average sacrificial layer aspect ratio (which is given by the lateral undercutting divided by the thickness of the sacrificial layer) of, but not limited to 125. By using crosslinked PMMA as the sacrificial layer, the dry release step has the benefits of being extremely quick at an etch rate of about 0.6 μm/s (crosslinked PMMA is easily ashed by oxygen plasma), simple, stiction-free, cheap and IC-compatible. Also, diffusion limitations that limit etching to short distances are commonly found when using wet etchants [23]. The low temperature (∼40–50°C) involved during the ashing step is useful for compatibility in standard IC processing and also avoids the accumulation of thermal stress caused by raised temperatures. Too high release temperatures may cause permanent plastic deformation of the structures. Because of the fact that crosslinked PMMA is transparent, this allows easy alignment for the next layer should one decide to use optical lithography for the mechanical layer. In addition, fig. 7(b)

shows that the resulting structures have low stress and do not buckle into the 160 nm high gap. This is believed to be as a result of the inert interface between the sacrificial layer and the mechanical layer where little inter-diffusion of ionic/atomic species occurs (which may cause stress gradients upon release). The low value of the Young's modulus of crosslinked PMMA (nominal PMMA has a modulus of around 5 GPa) enables itself to deform in order to provide stress relaxation for the rigid mechanical layers after their deposition.

Fig. 8 demonstrates some basic NEMS fabrication results using EBL [17]. Here, a quasi 3-D patterning of the crosslinked PMMA sacrificial layer is performed using EBL in a

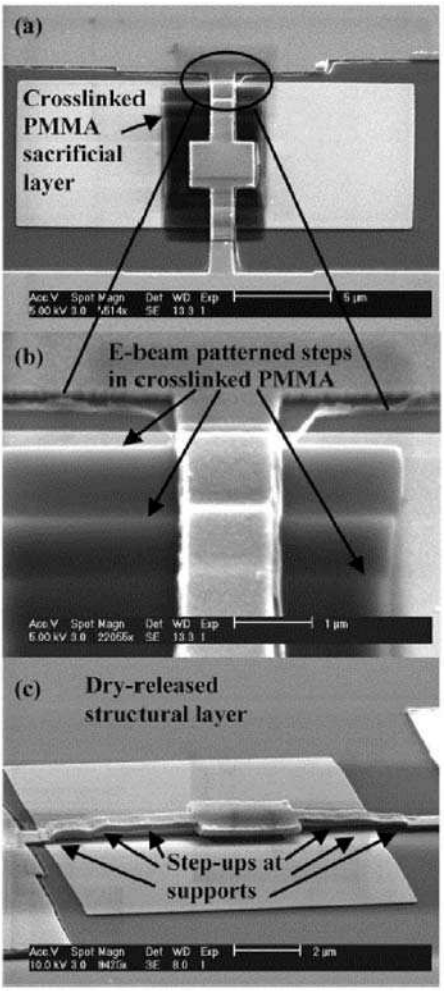

FIGURE 8. A demonstration of quasi 3-D surface nanomachining using crosslinked PMMA sacrificial layer. SEM micrographs showing (a) a Ti/SiO_2/Ni micro-paddle structure defined by EBL over a 400 nm thick crosslinked PMMA sacrificial layer, (b) how the paddle support structures climb over the multiple edge steps modulated by different levels of electron dose, and (c) a fully dry released suspended paddle structure. (From W.H. Teh *et. al.* (2003) *IEEE/ASME J. Microelectromech. Syst.*, **12**, 641–648. © 2003 IEEE. With permission.)

single process step. The additional z-direction degree of freedom in patterning the sacrificial layer provides flexibility in the mechanical design of NEMS. This is useful when designing nanomechanical filters, corrugated/ribbed structures and resonators. A micropaddle comprising of multi-layers 120 nm Ti/8 nm SiO_2/2 nm Ni measuring as low as 1 μm in lateral dimensions and suspended 400 nm above the substrate is realized. Deposition of the mechanical layer by thermal evaporation over the patterned sacrificial layer results in step-ups at the support. Fig. 8(b) shows an SEM micrograph on how the micro-paddle support structures climb over the multiple edge steps modulated by the different levels of electron doses with fig. 8(c) showing the final released low stress structure.

Fig. 9 shows various examples of microfabrication using crosslinked PMMA surface nanomachining over a 400 nm gap [17]. Figs. 9(a) and (b) respectively show SEM micrographs of low stress and released 1 μm (w) × 11 μm (l) × 130 nm (t) Ti/SiO_2/Ni bridge structures and 2 μm (w) × 5 μm (l) × 130 nm (t) Ti/SiO_2/Ni cantilever structures.

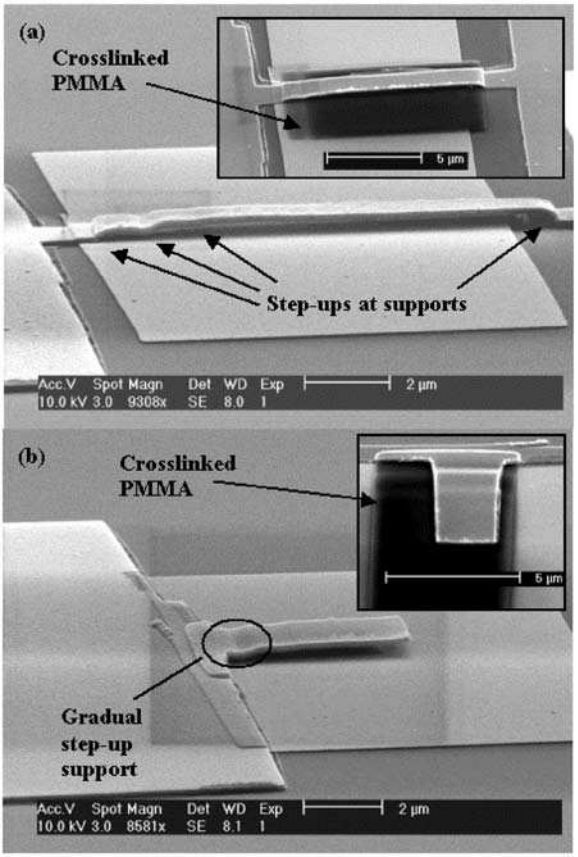

FIGURE 9. Other examples of microfabrication using crosslinked PMMA surface nanomachining over a 400 nm gap. SEM micrographs of dry released (a) 1 μm (w) × 11 μm (l) × 130 nm (t) Ti/SiO_2/Ni bridge and (b) 2 μm (w) × 5 μm (l) × 130 nm (t) Ti/SiO_2/Ni cantilever. Both insets show the corresponding unreleased structures. (From W.H. Teh *et. al.* (2003) *IEEE/ASME J. Microelectromech. Syst.*, **12**, 641–648. © 2003 IEEE. With permission.)

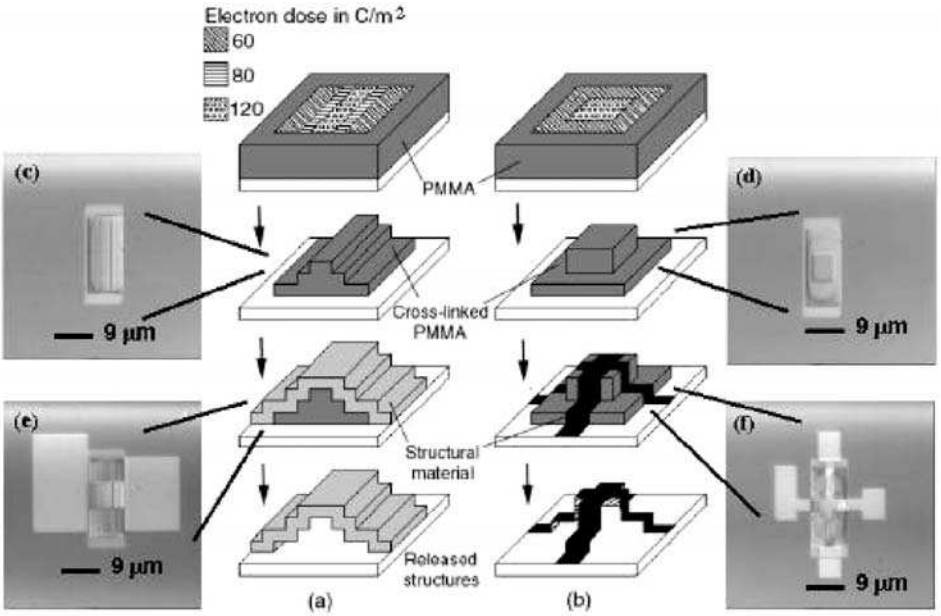

FIGURE 10. Quasi 3-D fabrication process of Au (53 nm) on Ti (7 nm) micro/nanomechanical structures using electron beam crosslinked PMMA as the sacrificial material. Relevant optical micrographs accompany selected process steps. The distinct step-ups formed by variable dose EBL in a single run confirm the quasi 3-D capability of this developed technique. (From W.H. Teh *et. al.* (2003) *J. Vac. Sci. Technol. B*, **21**, 3007–3011. © 2003 American Institute of Physics. With permission.)

In fig. 9(b), a gradual step-up support is realized when one reflows the crosslinked PMMA sacrificial layer at 150°C for several mins after patterning the steps located at the edge [see fig. 6(d)]. By means of reflowing, these corrugated steps will be smoothen and as a result, provide good step coverage for the supporting anchor of the cantilever. Besides the structural materials mentioned, other metallic layers such as Al, Au, Ti and electroplated Ni have been successfully tested as mechanical layers combined with crosslinked PMMA as a sacrificial layer. This is shown in the following figs. 10–13.

Figure 10(c)–(f) show relevant optical micrographs accompanying selected process steps for the two examples of EBL patterned Au (53 nm) on Ti (7 nm) structures: a bridge and a cross-membrane [18]. Here, 4 layers of PMMA MW 495 K on a Si substrate are used. The PMMA layers are ultimately crosslinked with different doses (60, 80 and 120 C/m^2) to give a final gap, measured from the highest point, of about 490 nm [see fig. 10(c)] and 410 nm [see fig. 10(d)]. The mechanical materials used are vacuum evaporated Ti (7 nm)/Au (53 nm) and are released isotropically using oxygen plasma at 100 sccm O_2 as before. As can be seen from figs. 10(c) and (d), the distinct step-ups formed by variable dose EBL in a single run confirm the quasi 3-D capability of this developed technique. These step-ups are then transferred to the mechanical layer by thermally evaporating thin layers of the structural materials (followed by lift-off), as shown in figs. 10(e) and (f). Clearly, for a better transfer, a conformal deposition technique such as sputtering is preferred. The fabrication results of the process schematic in fig. 10 are presented in figs. 11 (pre-release)

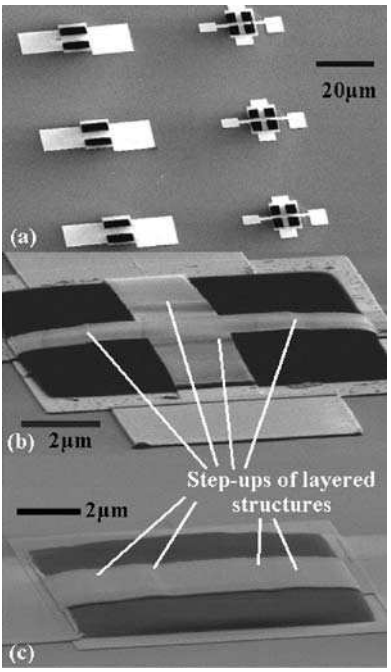

FIGURE 11. SEM micrographs of (a) an array of electron beam patterned pre-released cross-membranes and bridges with (b) and (c) showing the respective magnifications to reveal the step-ups of the layered structures. (From W.H. Teh *et. al.* (2003) *J. Vac. Sci. Technol. B*, **21**, 3007–3011. © 2003 American Institute of Physics. With permission.)

and 12 (after release) in the form of SEM micrographs. Fig. 11(a) shows an array of EBL patterned pre-released cross-membranes and bridges with figs. 11(b) and (c) showing the magnified step-ups of the layered Ti/Au structures. Fig. 12(a) shows the released 60 nm thick Ti/Au cross-membranes with supports measuring 8 μm long and 2 μm wide while fig. 12(b) shows the fabricated bridges measuring 10 μm long and 5 μm wide. As can be seen from fig. 12(b), reflowing effects on the crosslinked PMMA are transferred to the mechanical layer, making the step-ups not as clear as those in fig. 8.

Fig. 13 shows a composite SEM micrograph of some examples of metallic MEMS/NEMS devices fabricated using the crosslinked PMMA surface nanomachining

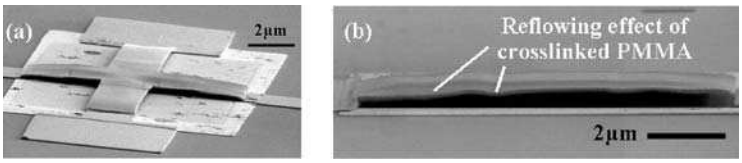

FIGURE 12. SEM micrographs of released 60 nm thick Ti/Au (a) cross-membranes with supports measuring 8 μm long and 2 μm wide, and (b) bridges measuring 10 μm long and 5 μm wide. The bridge and the cross-membrane are suspended about 490 nm and 410 nm above the substrate, respectively. (From W.H. Teh *et. al.* (2003) *J. Vac. Sci. Technol. B*, **21**, 3007–3011. © 2003 American Institute of Physics. With permission.)

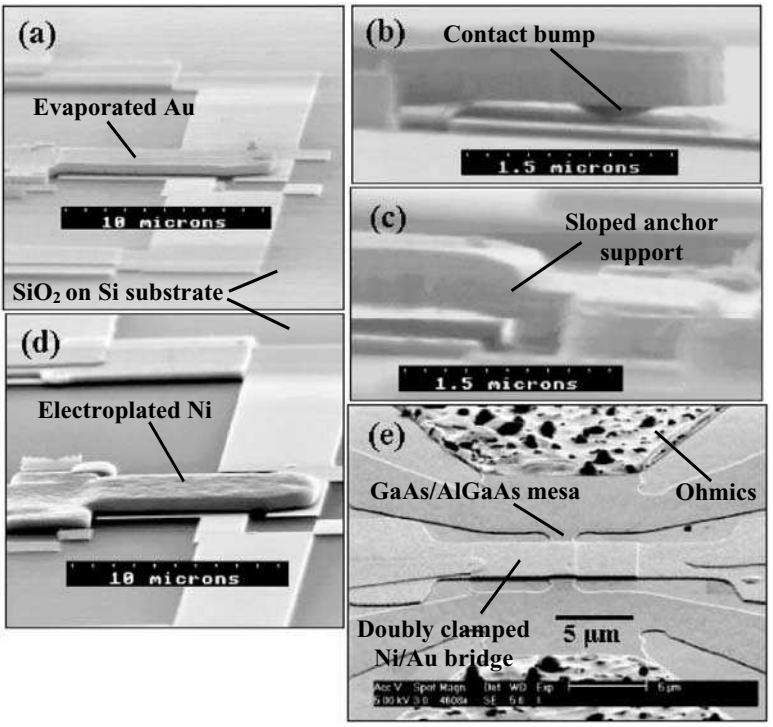

FIGURE 13. Examples of metallic MEMS/NEMS devices fabricated using crosslinked PMMA surface nanomachining. SEM micrographs show (a) a Au micromechanical switch, with (b) and (c) taking a closer look at its contact bump and its sloped edge respectively. (d) and (e), respectively, show a Ni micromechanical switch and a suspended Au bridge over a GaAs/AlGaAs mesa. All structures are typically low-stress and have near-zero curvature.

method [18]. Fig. 13 (a) shows an SEM micrograph of a three-terminal Au micromechanical switch, which uses electrostatic force for its actuation while figs. 13 (b) and (c) show a magnified view of its contact bump and sloped edge, respectively. When a high enough potential difference is applied between the cantilever beam and the bottom gate, the cantilever beam will deflect and snap down making contact with the landing electrode. The contact made will provide an electrical path from the anchor of the metallic cantilever beam to the landing electrode via the beam. This concept helps to realize an electrostatic micromechanical ohmic switch or relay. Fig. 13(d) shows an SEM micrograph of a three-terminal Ni micromechanical tunneling switch, which is also electrostatically driven. This micromechanical switch works by using the principle of electron tunneling between the contacted surfaces through a dielectric layer, which is positioned at the bottom of the contact bump. There are several advantages of this configuration as compared to the previous ohmic-based Au micromechanical switch such as having higher reliability and repeatability. More details of this particular working device are provided in subsection 3.1. A further example of the capability of this method involves the fabrication of a prototype floating-gate device based on a suspended Au bridge ($\sim$115 nm thick) over a GaAs/AlGaAs substrate, which contains a 70 nm deep 2-D electron system (2DES) [see fig. 13(e)], to be used as

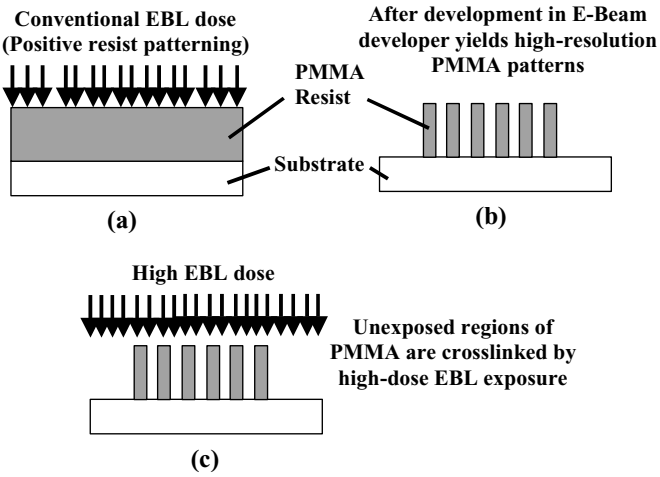

FIGURE 14. General schematic diagram showing a high resolution crosslinked PMMA patterning technique involving two exposure stages of the PMMA resist. With this technique, the resolution of the process is determined by the first stage, that is, the conventional (positive) patterning of PMMA.

a highly-sensitive deflection sensor. This device is suspended only about 80 nm over the patterned mesa using the developed surface nanomachining method [32].

It should be noted that the disadvantage of using EBL crosslinked PMMA as a negative (and sacrificial) resist, lies in its limited, albeit comparatively high resolution. This is due to proximity effects, associated with backscattered and secondary electrons exacerbated by the high dose exposure, which limits the line width to approximately 150 nm. Zailer *et. al.* [30], who used crosslinked PMMA as a dielectric layer for his experiments, proposed a high resolution technique involving two exposure stages of the PMMA. A schematic of this two-stage technique is illustrated in fig. 14. In the first stage, regions of the PMMA that are to be removed are exposed to standard EBL dose (4–9 C/m^2) [see fig. 14(a)] so that after development [see fig. 14(b)] only the unexposed regions remain. In the second stage, these unexposed regions are crosslinked by high-dose exposure [see fig. 14(c)]. Hence, the resolution of the process is determined by the first stage, that is, the conventional (positive) patterning of PMMA. As a trade-off for higher-resolution in patterning the sacrificial layer, more steps are therefore needed. Another disadvantage is the longer time required for EBL patterning (in the negative-tone) due to the extremely high dose required to crosslink the PMMA layers. This makes it practically unrealistic to pattern whole wafers.

3. SELECT APPLICATIONS RESEARCH

This section reports on the use of low dimensional EBL crosslinked PMMA sacrificial layer for applications research such as MEMS/NEMS devices that act as sensors and actuators. In subsection 3.1, the fabrication and electrostatic actuation of one of the smallest near-zero curvature Ni micromechanical tunneling switch is presented [33–35]. The use of electrostatic pressure to modulate the tunneling current characteristics of the switch based on

an elastic compressible contact surface model is demonstrated [35]. Subsection 3.2 reports a simple methodology to enable the integration of high yield, uniform and preferential growth of vertically-aligned carbon nanotubes (VACNTs) on micro/nanomechanical structures [36, 37]. This technique uses a combination of EBL crosslinked PMMA surface nanomachining and direct current plasma enhanced chemical vapor deposition (dc-PECVD) of carbon nanotubes [36, 37]. Here, selective placement of high yield and uniform VACNTs on a partially suspended $Ti/SiO_2/Ni$ microstructure has been demonstrated [36, 37]. A final example of applications research enabled by using crosslinked PMMA as the sacrificial layer is the fabrication of thermal microactuators by EBL. A brief description of these thermally-actuated micromechanical devices is reported in subsection 3.3.

3.1. Development of Electrostatic Ni Micromechanical Tunneling Switches

NEMS clearly represent an emerging enabling technology, important for both fundamental and applied research. Some of the earliest work concerning the fabrication of nanomechanical structures for fundamental research includes the first demonstration of sub-micron free standing structures [38], the first investigation of 1-D phonons in free standing 1-D wires [39], the first free-standing GaAs wires [40] and the first resonator measurements on sub-micron free-standing wires [41]. More recent applications of NEMS for fundamental physical studies include investigations on the quantum of nanoscale thermal transport [42] and the detection of quantum mechanical actuation by the Casimir Force [43]. As for applications research, NEMS has facilitated the development of ultra-sensitive sensors such as the mechanical magnetic resonance imager [44] and the nanomechanical electrometer [45].

While electrostatic based mechanical systems in the order of many tens/hundreds of microns have been developed to be applied as microswitches and microrelays [13, 46–51], work on the scalability of similar devices to below 10 μm in length and submicron in thickness remains largely unexplored. One of the main reasons for this is the difficulty in controlling the residual stress in ultra-thin films, especially for metallic films, which tend to warp upon release [52, 53]. A well-controlled mechanical profile is important to produce a consistent and reproducible switching behavior. Because of their high reflectivity and conductivity, the ability to fabricate near-zero curvature metallic cantilevers in a scale that bridges typical MEMS and NEMS dimensions can be useful in force spectroscopy and high-resolution surface imaging. This is due to the high levels of light at the detector, which increase the signal-to-noise ratio of the measurements. In addition, flat and suspended NEMS metallic structures can be used as floating gates (due to their conductive nature) to couple electric field locally with low-dimensional (0-D, 1-D or 2-D) electron systems for both basic and applied research [6, 32].

Other authors [13, 48] have reported recipes for fabricating working nickel microswitches with typical dimensions of 30 μm wide, 1 μm thick and 65 μm long suspended about 1.5 μm above the gate. This large footprint is however, undesirable when it comes to integration with CMOS electronics. Meanwhile, other attempts in fabricating metallic microrelays usually result in having a high mechanical curvature and high electrical hysteresis [54]. Consequently, this subsection describes a near curvature-free surface nanomachined Ni cantilever beam that forms part of a three-terminal micromechanical tunneling switch [33–35], which is about 325 times smaller in terms of volume as compared to those previously

reported [13, 48]. The tunneling switch is fabricated using EBL crosslinked PMMA and electroplated nickel as the sacrificial layer and the main structural material, respectively. By switching to high electron doses to crosslink selected regions of PMMA to be used as the sacrificial layer, provides the merits of combining EBL defined mechanical and sacrificial layer in the same step [34]. In addition, the compliance nature of a polymeric-based sacrificial material in the form of crosslinked PMMA (as a result of having a low Young's modulus) allows the stress relaxation of the subsequently deposited mechanical layer. The fabricated tunneling switch uses an insulating barrier between two Au contacts to avoid short-range metal-metal forces, which typically cause contact adhesion failure as well as high hysteretic behavior during on-off switching.

A schematic of the process steps to fabricate suspended Ni micromechanical structures using crosslinked PMMA quasi 3-D surface nanomachining is summarized in each part of fig. 15. Fig. 16 illustrates relevant optical micrographs that accompany selected process steps. A more detailed description of the process can be found elsewhere [33]. To fabricate the device, SiO_2/Si wafers were used as the insulating substrate. 15 nm NiCr/90 nm Au films are thermally evaporated and patterned via lift-off using optical lithography to define the bond pads and the connecting metallization lines to the device active area. This is followed by the definition of the lower metal layer, which forms the source, gate and drain electrodes, using thermally evaporated 7 nm NiCr/30 nm Au films on conventional EBL patterned PMMA resist and then lifted-off [see fig. 15(a) and 16(a)]. Next, the first sacrificial layer of PMMA (0.4 μm) is spun on [see fig. 15(b)] and crosslinked using a high electron beam dose of 120–150 C/m^2 to set the deflection distance [see fig. 15(c) and 16(b)]. As described earlier, the effective thickness of the PMMA resist reduces by around 45–50% after complete crosslinking due to the removal of side chains of the molecules and the evaporation of volatile by-products. A second sacrificial PMMA layer is then spun on and patterned over the first one to set the contact tip protrusion distance. Preceding the second crosslinking, a notch to be used as a receptacle for the contact tip, is patterned by conventional EBL (with a dose of 9 C/m^2) right above the drain electrode [see fig. 15(d)]. This step in the fabrication process is similar to the generic two-stage technique shown in fig. 14. The device is then placed on a hot plate at 60°C for 30 mins followed by 150°C for 5 mins to reflow the PMMA layers to allow the formation of a sharper beam tip and a better edge shape [see fig. 17]. This also enables the effective contact area of the tip to be reduced below the patterned dimensions. To define the mechanical structure, thin Al (3 nm) and Au layers (30 nm) are evaporated on conventional EBL patterned PMMA resist (in the shape of a cantilever) and then lifted-off [see fig. 15(e)]. Using Al as the tip contact material exploits the fact that aluminum oxide is formed *in-situ* during the dry release step in oxygen plasma while Au serves as the seed layer for the subsequent electroplating of Ni. By using a nickel sulphamate bath containing 300 g/l of nickel sulphamate $Ni(SO_3NH_2)_2.4H_2O$, 10 g/l of nickel chloride $NiCl_2.6H_2O$ and 40 g/l of boric acid H_3BO_3, the main Ni mechanical layer is electroplated on the previously EBL patterned Au seed layer [see fig. 15(f) and 16(c)]. In the last step, the Ni beam structures are dry released isotropically in oxygen plasma by etching off the crosslinked PMMA sacrificial layers [see fig. 15(g) and 16(d)] resulting in three-terminal micromechanical devices. Plasma oxidation offers non-stiction dry release and the right amount of oxidation needed for the thin Al layer. Being fast, straightforward, and production friendly, it is also the favored method for producing magnetic tunnel junction (MTJ) material [55]. The micromechanical tunneling switch shown schematically in

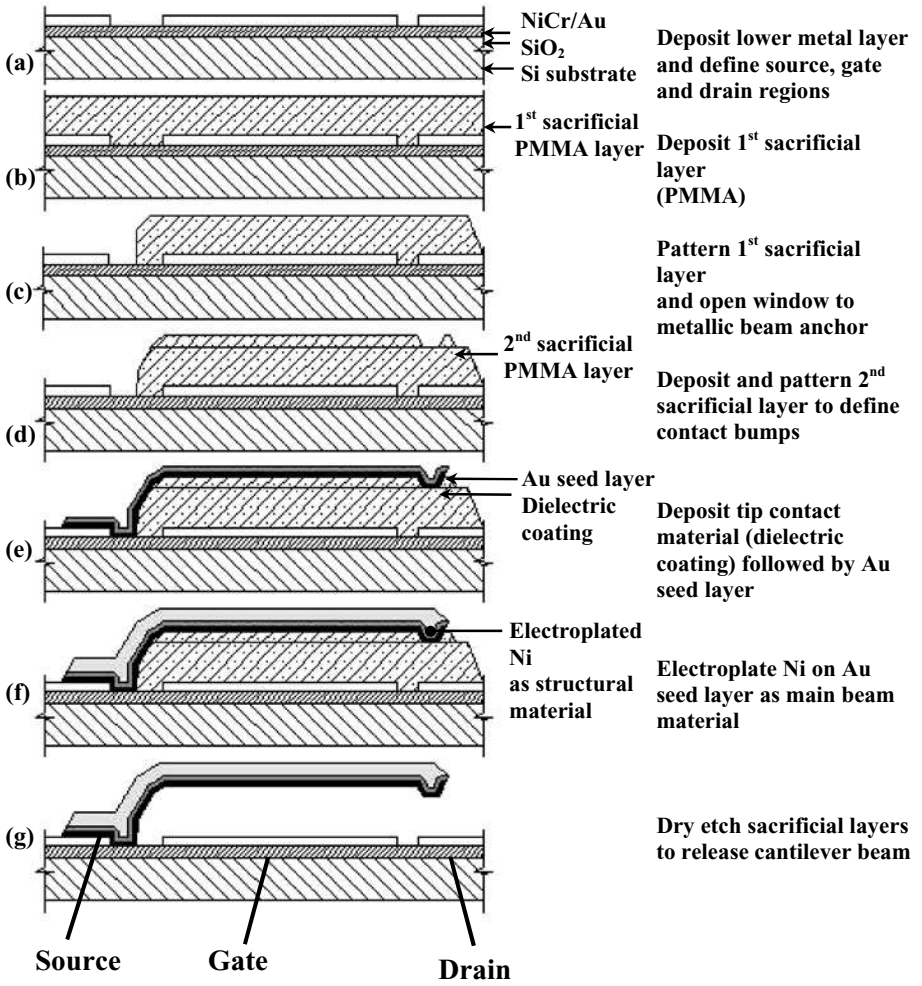

FIGURE 15. Cross sectional diagrams of the micromechanical tunneling switch at various stages during the fabrication process using electron beam crosslinked PMMA surface nanomachining and nickel electroplating. (From W.H. Teh *et. al.* (2003) *J. Micromech. Microeng.*, **13**, 591–598. © 2003 IOP Publishing Ltd. With permission.)

fig. 15(g) takes the form of a Ni cantilever beam, which is the moving element, affixed at one end and free to oscillate at the other. The lower part of the beam is coated with an insulator (aluminum oxide, in this case), which is thick enough to reduce metal-metal bonding, yet thin enough to yield electron tunneling. The concept of a tunneling switch avoids some of the contact sticking problems encountered in ohmic contact switches. When a potential difference is applied between the gate and the beam (source), the resultant electrostatic force pulls the cantilever beam down. At a specific pull-in voltage (V_{pi}), contact between the beam (source) and the landing electrode (drain) is made. Switch closure allows a metal-insulator-metal (MIM) tunneling junction to be mechanically formed so that when there is an applied potential difference between the source and the drain, electrons at the metal Fermi energy

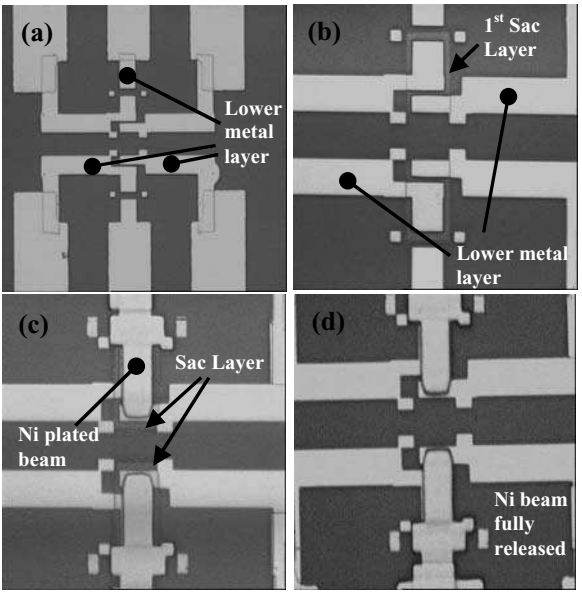

FIGURE 16. Plan view of optical micrographs showing (a) the lower NiCr/Au (7 nm/30 nm) metal layer leading to the source, gate and drain electrodes, (b) deposition and crosslinking of the first PMMA sacrificial layer, (c) a pre-released nickel plated beam, and (d) a fully dry released nickel plated beam using oxygen plasma ashing. (From W.H. Teh *et. al.* (2003) *J. Micromech. Microeng.*, **13**, 591–598. © 2003 IOP Publishing Ltd. With permission.)

can tunnel through the insulator. This is seen as an abrupt rise in the source current as the circuit is completed due to electron conduction via the Ni micromechanical beam.

The process description given above has led to the fabrication of $l = 10$ μm long, $b = 4$ μm wide, near zero-curvature Ni/Au/Al_2O_3 cantilever beam structures, suspended over a nominal gap of $g = 0.43$ μm, with plated Ni ranging from $t_{Ni} = 0.15$ to 0.40 μm thick on a $t_{Au} = 30$ nm Au seed layer. Subsequent SEM inspections [see fig. 18] reveal no significant indication of curvature for the plated Ni beams. It is believed that the

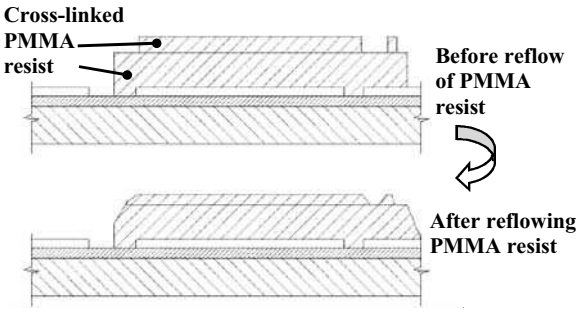

FIGURE 17. Schematic illustrations showing the reflow of PMMA resist to reduce tip contact area and also to improve slope of the PMMA resist sidewalls. (From W.H. Teh *et. al.* (2003) *J. Micromech. Microeng.*, **13**, 591–598. © 2003 IOP Publishing Ltd. With permission.)

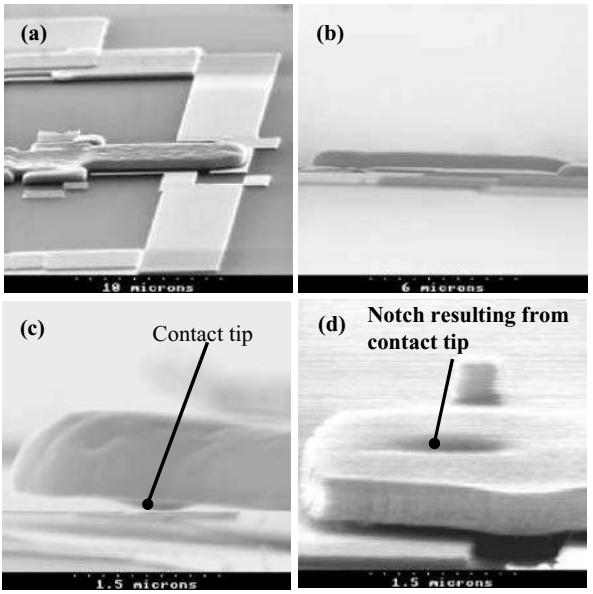

FIGURE 18. SEM micrographs of fabricated tunneling switch (a) in the perspective view (b) in the edge-on view, demonstrating near-zero curvature (c) with a close-up of its contact bump and (d) with its electron beam lithographically defined notch. (From W.H. Teh *et. al.* (2003) *J. Vac. Sci. Technol. B.*, **21**, 2360–2367. © 2003 American Institute of Physics. With permission.)

near-zero curvature profile results from the low-stress Ni plating process, in which further stress relaxation of the Ni deposits is provided by the complaint crosslinked PMMA sacrificial layer. The crosslinked PMMA simply deforms to stress-relax the Ni deposits.

The DC switching characteristics for various thicknesses (0.15 μm to 0.40 μm) of plated Ni cantilever beam are shown in fig. 19(a). The switching characterization is performed by sweeping the gate voltage (V_g) linearly while holding the drain voltage (V_d) at a constant 3.0 V with the source (V_s) electrode grounded [34] in a low pressure (<1 mbar) environment. Switching path for all devices is similar to that of the 0.35 μm thick Ni beam, that is, in the direction of the arrows. The results of fig. 19(a) show that thicker cantilever beams require a higher pull-in voltage than thinner beams and also, high off state/on state isolation between the cantilever beam and the gate was achieved with resistance values of more than 10^{12} Ω. More importantly, as evident from the results shown in fig. 19(a), the overall low hysteretic nature (∼0.5 to 4.5 V) of the switches suggests relatively lower adhesive forces between the tip contact material (Al_2O_3) and the landing drain electrode (Au) as compared to when Au-Au contacts were used. When Au-Au contacts were used, a very large hysteretic behavior is obtained and in the worst case, the switch remains stuck once switched on [34]. From the life-time test, these switches show a fairly consistent pull-in voltage where in the worst case, the pull-in voltage and the pull-out voltage for the 0.28 μm plated Ni beam only change about 4% and 11% from their respective initial values of 37 V and 35 V after switching for up to 1 billion times [34]. This implies that no significant permanent physical change (i.e. plastic deformation) to the beam has resulted from the test and this result reinforces the reliability of the repeatability of its switching characteristics.

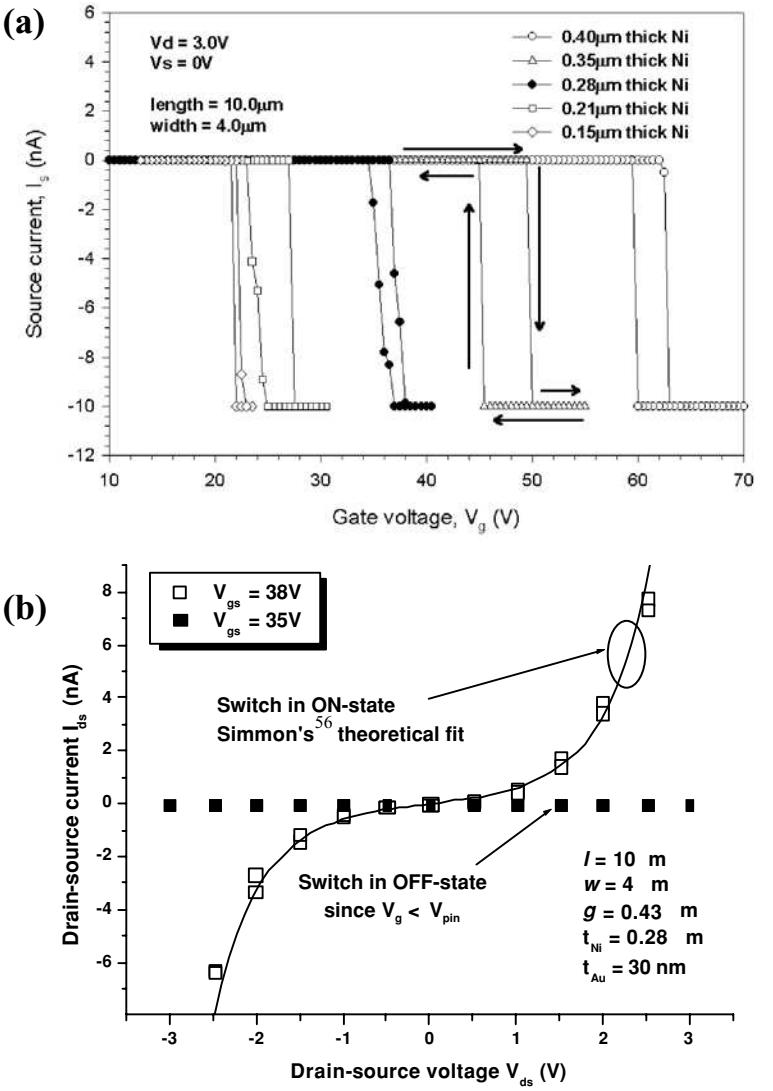

FIGURE 19. Switching characteristics of electrostatic Ni micromechanical tunneling switch: (a) DC switching behavior for 10.0 μm long, 4.0 μm wide Ni/Au/Al_2O_3 cantilever beams with different plated thickness (0.15 μm to 0.40 μm) of Ni in an air ambient pressure of < 1 mbar and a current limit of ± 10 nA. Switching path for all devices is similar to that of the 0.35 μm plated Ni micromechanical switch, as shown by the arrow lines and (b) an example of an I_{ds}–V_{ds} tunneling curve, fitted with Simmons theory when the gap between the cantilever tip and drain electrode is closed, with $V_{gs} = 38$ V. When V_{gs} is below V_{pin} (i.e. 35 V), no source current is detected. (From W.H. Teh *et. al.* (2003) *J. Vac. Sci. Technol. B.*, **21**, 2360–2367. © 2003 American Institute of Physics. With permission.)

In fact, by having a process that uses crosslinked PMMA sacrificial layer in combination with Ni electroplating, which is able to repeatedly produce these near-zero curvature cantilevers, the reliability of predictions of device behavior is enhanced. In addition, the reliable near-zero curvature properties of the metallic beams allow low switching voltages to be achieved. As for the tunneling behavior of the switch, this can be clearly seen from fig. 19(b), where an applied gate voltage V_{gs} of 38 V (which is beyond V_{pin}) causes the tip of the Ni beam to contact the underlying Au electrode (drain) due to instability to create a dielectric sandwich of $Au/Al_2O_3/Au$. When this happens, the I_{ds}–V_{ds} characteristics becomes non-linear and the contact can be modeled as a tunnel junction based on Simmon's [56] theory where two gold electrodes are separated by a thin Al_2O_3 layer. Electrical symmetry as seen from the I–V characteristics indicates structural symmetry in the barrier and its interfaces with the metal electrodes, and thus, by implication, it is believed that a full oxidation of the 3 nm Al film has resulted from the *in-situ* plasma reaction during the dry release step.

Figure 20(a) shows the drain-source current (I_{ds}) as a function of the drain-source voltage (V_{ds}) for different applied gate voltages (V_{gs}) ranging from 35 V up to 42 V. It demonstrates the compressibility of the contact surfaces by resulting in higher tunneling current as the electrostatic pressure induced by the gate voltage increases. At a gate voltage of 35 V, no tunneling current or field emission flows between the source and drain, reinforcing the predicted pull-in instability, which states that the beam snaps down after deflecting about one-third of the initial gap. This discontinuous deflection behavior prevents tunneling in the OFF-state when there is a large gap. In addition, by plotting I_{ds} against V_{gs} [see fig. 20(b)], it can be seen that the tunneling current is an approximate linear function for the range of applied gate voltages (36–42 V) discussed, with a larger linear dependence as the drain-source voltage increases. This ranges from 0.03 nA/V at $V_{ds} = 0.5$ V to 0.46 nA/V when V_{ds} is increased to 2.5 V for different V_{ds}. This is an important observation because it shows that the drain-source current is dependent on the gate voltage due to the compressible nature of the contact surface. As V_{gs} increases, more forces are being applied at the tip, which results in the increase in the effective tunneling area. The increase in tunneling area leads to the increase in I_{ds} as shown in fig. 20. Further details on the demonstration of the use of electrostatic pressure to modulate the tunneling current characteristics of a micromechanical tunneling switch based on an elastic compressible contact surface model can be obtained from ref. [35]. In summary, a surface nanomachined micromechanical Ni tunneling switch fabricated using electroplated Ni and electron beam crosslinked PMMA with dimensions in the few-micron regime has been presented. This technique has been most suitable and flexible for the fabrication of the tunneling switch as described above.

3.2. Integration of Vertically Aligned Carbon Nanotubes on Low-Stress Micro/Nanomechanical Structures

Using MEMS fabrication technologies, or variations of these, it is indeed possible to realize a variety of microscopic sensors and actuators. It cannot be denied that the unique interdisciplinary nature of micro/nanomachining techniques and their applications can and does lead to exciting synergies. However, only using these techniques to fabricate microcomponents has yet to realize the full potential of MEMS/NEMS. It is equally important to

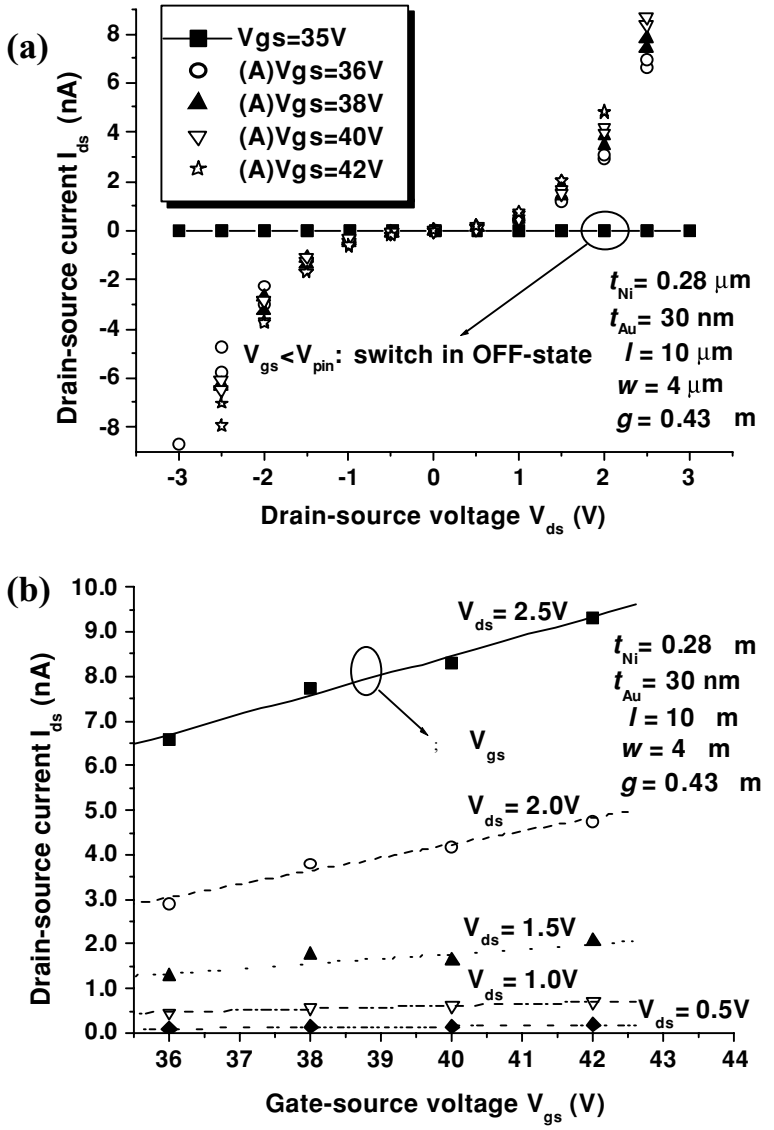

FIGURE 20. Reversible electrostatic control of micromechanical structure tunneling characteristics: (a) Measured I–V characteristics for different applied gate voltage V_{gs} on a linear-linear scale and (b) Drain-source tunneling current I_{ds} plotted as a function of the applied gate voltage V_{gs} for different drain-source voltages V_{ds}. (From W.H. Teh *et. al.* (2003) *J. Appl. Phys.*, **94**, 4614–4618. © 2003 American Institute of Physics. With permission.)

be able to open up the field of integrating MEMS/NEMS structures with nanotechnology, which is critical to the advancements of MEMS/NEMS in the 21st century.

It is desirable to incorporate carbon nanotubes (CNTs) onto MEMS/NEMS for various fundamental research and potentially important technological applications. The coupling of micron scale mechanical component, which typically exhibit nanometer scale translational

precision with the remarkable structural, electrical, and mechanical properties of CNTs, will greatly enhance MEMS performance as sensors in mechanical, electrochemical, biological or electronic applications [57]. The feasibility of growing vertically-aligned carbon nanotubes (VACNTs) using plasma enhanced chemical vapor deposition (PECVD) was first reported by Ren *et. al.* [58]. Since then, this technique has been extensively developed to be a well-controlled and preferred method to produce highly uniform CNTs in terms of alignment, diameter and length [59]. With this capability, VACNTs have emerged as highly promising field emitters in applications such as scanning probes, displays, microwave amplifiers and parallel EBL [59]. In the literature, reported attempts to integrate CNTs into electronic devices and electromechanical systems include: patterned growth of CNTs to bridge predefined molybdenum electrodes [60], placement of a CNT onto a MEMS structure using a hybrid atomic force microscope/scanning electron microscope (AFM/SEM) system [57], demonstration of wafer scale production of CNT scanning probe tips by selectively placing catalysts on prefabricated Si tips [61], the fabrication of an on-chip vacuum microtriode using CNT field emitters and MEMS design/fabrication principles [62], and more recently, the incorporation of CNTs torsional springs into nanometer scale mechanical devices [63].

Consequently, this subsection reports a simple methodology to enable the integration of high yield, uniform and preferential growth of VACNTs on micro/nanomechanical structures. This technique uses a combination of EBL crosslinked PMMA surface nanomachining and direct current plasma enhanced chemical vapor deposition (dc-PECVD) of multi-walled CNTs. In this work, selective placement of uniform VACNTs on suspended $Ti/SiO_2/Ni$ microstructures has been demonstrated. This integration scheme demonstrates the versatility of EBL crosslinked PMMA as a low-dimensional sacrificial layer. A detailed description of this integration process can be found in refs. [36] and [37] where it was first reported. This integration approach affords VACNT-micromechanical devices without any post-growth processing (which can cause damage to the nanotubes during microfabrication), and will find applications in NEMS.

The generic schematic for the integration of VACNTs on suspended $Ti/SiO_2/Ni$ microstructures is shown in fig. 21. For easy readability, the fabrication process for selected MEMS/NEMS structures comprising of the material system $Ti/SiO_2/Ni$, which were previously reported in subsection 2.4 will be briefly repeated. However, this time, the microstructures are further processed to be used as 'scaffolds' for the growth of the VACNTs. The process starts with a (100) antimony-doped n^{++} Si wafer substrate with nominal resistivities measuring between 3–10 Ω cm. After cleaning with hydrofluoric acid, two layers of PMMA are spun on one after the other, both at 6000 rpm for 50 s. The first spun-on layer is baked for 10 mins at 150°C and the subsequent one for 30 mins immediately after. Regularly spaced 50 μm $\times$ 50 μm squares are then selectively crosslinked onto the bilayer PMMA by EBL with a 25 kV accelerating voltage, a current of 300 pA and a dose of 120 C/m^2 using a modified Hitachi S800 SEM [see fig. 21(a)]. After dissolving the unexposed PMMA in acetone, crosslinked PMMA square grids remain behind [see fig. 21(b)]. After exposure, the thickness of the PMMA reduces by around 50% and is measured to be about 200 nm and this sets the effective thickness of the sacrificial layer. To produce desirable edge slope so that the thermally evaporated structures can easily climb over the crosslinked PMMA layer, a reflow treatment of 30 mins at 60°C and 5 mins at 150°C is performed [see fig. 21(c)]. Reflowing reduces the thickness by a further 5–8 nm. The process then proceeds with the

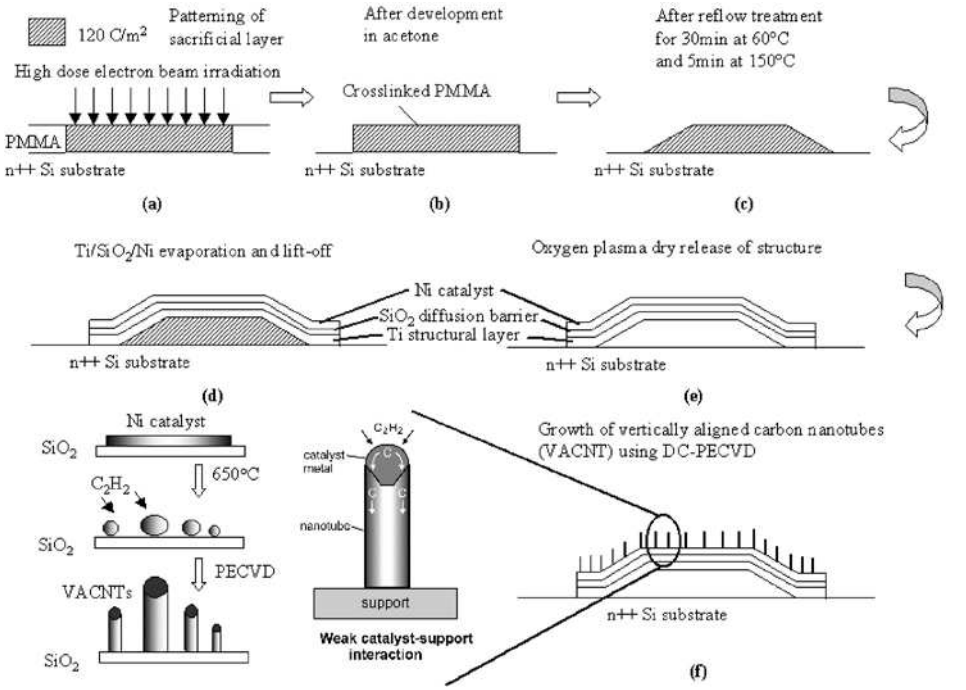

FIGURE 21. Synthesis of uniformly patterned vertically-aligned carbon nanotubes (VACNTs) on low stress micro/nanomechanical structures. (a, b) spin-coated PMMA is selectively crosslinked by a high dose of electron beam irradiation to form the highly compliant sacrificial layer. (c) when necessary, the crosslinked PMMA sacrificial layer is reflowed to produce a gradual edge slope. (d) deposition of the Ti main structural layer followed by the thin SiO_2 diffusion barrier and the Ni catalyst layer. (e) quick dry release of the structure using oxygen plasma ashing. (f) selective growth of VACNTs via the tip-growth mechanism using the dc-PECVD technique. (From W.H. Teh *et. al.* (2003) in *Proc. of the 12th Int. Conf. on Solid-State Sensors, Actuators and Microsystems (Transducers 2003)*, **1**, 190–193. © 2003 IEEE. With permission.)

subsequent patterning of the cross structures using optical lithography, which is aligned over the crosslinked PMMA sacrificial layers. The transparent nature of the thin PMMA sacrificial layers allows easy alignment during the optical lithography step. A 180 nm thick layer of Ti is thermally evaporated followed by magnetron sputter-deposited 8 nm SiO_2 film and 3.5 nm Ni film. Standard lift-off in acetone follows [see fig. 21(d)]. In the final step before CNTs growth, the Ti/SiO_2/Ni structures are dry released using isotropic oxygen plasma for 55 s [see fig. 21(e)]. Fig. 22(a) and (b) respectively show SEM micrographs of an undeformed cross membrane microstructure before and after release.

The substrate is then loaded into the CNT deposition chamber and evacuated to a base pressure of 5×10^{-2} mbar. The substrate is heated up to 650°C in NH_3 with the plasma initiated by applying a dc bias of −600 V to the cathode. Subsequently, acetylene (C_2H_2) is introduced to form a 25% C_2H_2 in NH_3 mixture and the deposition is performed for 15 mins at a total pressure of 4 mbar in a stable discharge. At 650°C, the thin Ni film catalyst coalesced into nanoclusters [see fig. 21(f)], which seeded the growth of the CNTs via a tip-growth mechanism: the carbonaceous gas decomposes on the surface of the catalyst

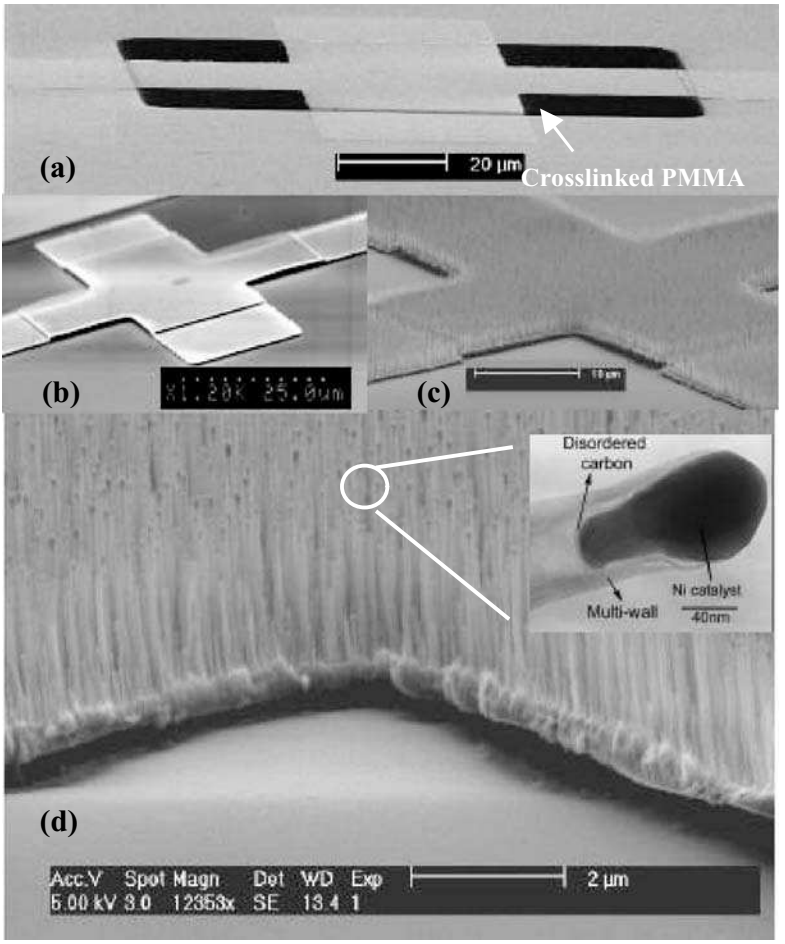

FIGURE 22. SEM micrographs of (a) a cross-membrane structure of 180 nm Ti/8 nm SiO_2/3.5 nm Ni thick on electron beam crosslinked PMMA sacrificial layer, (b) dry released of the same and (c, d) after VACNTs growth using dc-PECVD technique. The low stress structure is suspended about 200 nm above the substrate. Inset of (d): a TEM micrograph of one of the vertically-aligned multi-walled carbon nanotubes.

particle, the carbon diffuses across the particle under an activity gradient, and the carbon precipitates out on the opposite side. The thin SiO_2 film serves as a diffusion barrier to prevent Ni from diffusing into Ti. This diffusion barrier allows a better control of the availability of the catalytic material for CNT growth. The electric field in the plasma sheath guides the CNTs vertically during growth. This is where a conducting substrate is able to avoid arcing between the substrate and the Ti cross structure during the plasma generation. The successful growth of VACNTs is observed in figs. 22(c) and (d) where the previously free-standing Ti microstructures are now covered with a dense and uniform 'forest' of VACNTs highly selective to areas which contained the catalyst. A detailed description of the VACNTs growth using dc-PECVD and its dependence on various parameters can be found in ref. [64]. In summary, figs. 21(a)–(e) show the schematic of the EBL crosslinked PMMA

surface nanomachining method used for the fabrication of the suspended microstructures while fig. 21(f) shows the schematic for the growth of the VACNTs using dc-PECVD.

Transmission electron microscopy (TEM) observations [see inset of fig. 22(d)] reveal that the deposited VACNTs were multi-walled CNTs measuring an average of 2 μm in length and 70 nm in diameter with the standard deviation of the distribution in height and diameter about 18%. This variation is a result of the large area of the Ni catalyst film, which coalesced to form multiple nanoclusters of different sizes and catalyzed the growth of 'uneven' CNTs. In addition, a Ni catalyst was observed at the tip of the tubular and mostly hollow VACNT, which contained 20–40 well crystallized graphene walls parallel to its axis. SEM investigations also reveal discontinuous tears at the edge of the supports particularly at the corners due to differential stress generated between the substrate and the Ti structure at the high growth temperatures (650°C). This is not surprising since the films are thinnest at the step-up edges due to the nature of thermal evaporation. Nevertheless, it can be concluded that the structures produced using crosslinked PMMA surface nanomachining have low stress and is not significantly affected by the high sintering temperatures even up to 650°C.

The growth of shorter VACNTs on NEMS structures is also attempted. For this purpose, process steps remain identical except this time, much smaller dimensions are being used for the mechanical structures (cantilevers: 2.5 μm × 1 μm × 130 nm; paddles: 3 μm × 3 μm with 1μm wide supports) [36]. These NEMS structures are 120 nm Ti/8 nm SiO_2/2 nm Ni thick and are suspended over a 430 nm gap above the substrate. Also, the VACNTs were grown for a much shorter period of 2 mins. This results in VACNTs with an average height of about 260 nm and an average diameter of about 37 nm. The shorter VACNTs are desirable in terms of integration with NEMS. An example of these results, as observed by the SEM is shown in fig. 23. Fig. 23 shows selectively grown VACNTs on a 2.5 μm

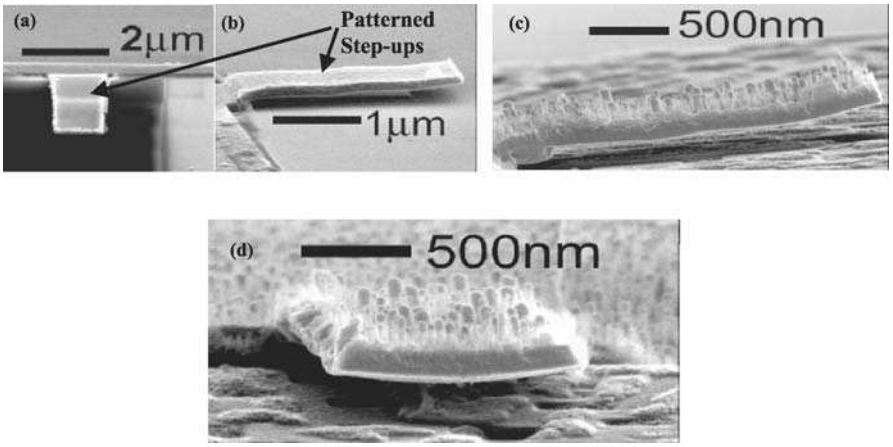

FIGURE 23. SEM micrographs of (a) an electron beam lithographically defined cantilever on crosslinked PMMA, (b) dry released of the same and (c, d) after VACNTs growth. The Ti/SiO_2/Ni cantilever measures about 2.5 μm × 1μ m × 130 nm over a 430 nm gap. The step-ups are patterned by using 2 different electron beam dose in a single run during crosslinking. (From W.H. Teh *et. al.* (2003) in *Proc. of the 12th Int. Conf. on Solid-State Sensors, Actuators and Microsystems (Transducers 2003)*, **1**, 190–193. © 2003 IEEE. With permission.)

(l) × 1 μm (w) × 130 nm (t) Ti/SiO_2/Ni cantilever suspended 430 nm above the substrate. From fig. 23, it can be seen that it is indeed possible to integrate short VACNTs on a post-processed NEMS structure. Nevertheless, some stress effects are noticeable in some of the mechanical structures, mainly caused by the high sintering temperatures involved during the VACNTs deposition. It is however believed that should the confinement of the thermal mismatch be localized to a small spot on the mechanical structure by patterning the oxide and the Ni catalyst into isolated square dots measuring 100 nm in width, this mismatch can be kept to a minimum. By doing so, it may be possible to grow 100% yield, VACNTs with an average standard deviation of 6%, resulting in a much tighter distribution in terms of height and diameter [59].

In conclusion, this work demonstrates the feasibility of integrating VACNTs selectively on low-stress post-MEMS processed microstructures. Here, an EBL crosslinked PMMA surface nanomachining technique together with dc-PECVD growth of VACNTs are used for the integration scheme. The motivation of the former is to exploit the compliance of crosslinked PMMA for stress relaxation of the mechanical structures while the latter is to produce vertically-aligned CNTs. The easy removal of crosslinked PMMA using oxygen plasma provides flexibility in terms of mechanical material choice. Further work is necessary to solve issues of reliability in this integration process, primarily due to differential stress generated during the high-temperature VACNTs growth. Again, EBL crosslinked PMMA has been demonstrated to be an important processing step to produce submicron gaps in an integration scheme that will hopefully create novel devices that incorporate nanotube architectures.

3.3. Development of Electro-Thermal Microactuators and its Applications

Thermal actuators are devices that utilize constrained thermal expansion of thin membranes to achieve an amplified motion. In contrast to electrostatic actuators, electrothermal actuators can produce larger forces, and hence, larger displacements, and thus, can find applications as micromanipulators in areas such as communications, space exploration and microbiology. Examples of applications based on thermal microactuators include: two-channel fiber optical switches [65], optical micromirror switches [66], multiple-contact electrical switches and microtweezers [67] and even polymeric microcages [70] to manipulate biological objects such as cells and microparticles. There have also been reports on the fabrication of walking microrobots based on the dynamic motion of an entire array of microcilia thermal actuators [69].

In principle, there are two basic types of thermal actuators: the in-plane motion, lateral thermal actuator based on the thermal expansion difference induced by temperature difference within a planar structure and the out-of-plane motion, vertical thermal actuator based on the thermal expansion difference between two materials of a bilayer structure. Examples of lateral thermal actuators include devices such as the heatuator [70] and the chevron [71]. Variations of these include the reverse use of heatuators [72] as well as the concept of a planar microspring actuator [73]. A general schematic of various types of thermal actuators is illustrated in fig. 24. The basic principle of a heatuator is based on the fact that when current flows from the thinner hot arm to the wider cold arm, the thinner arm is heated up more than the wider arm due to its higher resistance. As a result, it expands more than the cold arm, leading to a lateral deflection of the actuator [see fig. 24(a)]. The

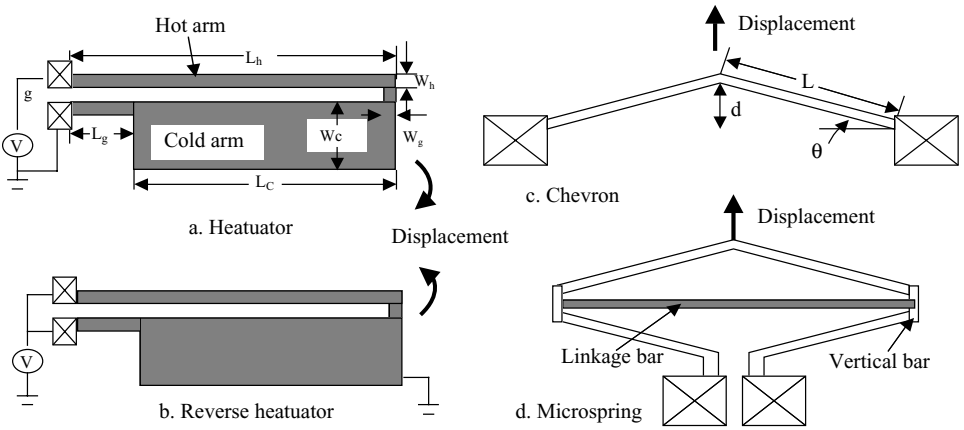

FIGURE 24. Schematic drawings illustrating (a) the conventional heatuator, (b) the reverse use of the heatuator, (c) the chevron microactuator, and (d) the microspring actuator.

deflection of a heatuator depends on the ratio of the length of the hot arm to the cold arm, the space between the arms, and the hinge length/width. Several heatuators can also be connected in parallel in order to produce a larger force [74]. The deflection of a reverse use heatuator is principally similar to that of a heatuator: as the voltage is being applied, the current finds a lower resistive path in the wider arm, generates a higher temperature so that the wider arm expands more, and consequently, the actuator deflects in the opposite direction [see fig. 24(b)]. By connecting these devices in series with the colder arms facing the inside or the outside, can produce microactuators with both contraction and expansion motion [71]. As for the chevron type lateral thermal microactuator, its basic design consists of two beams, which are held fixed between two rigid supporters [see fig. 24(c)]. As the current is forced through these beams, a temperature rise will occur and this results in the thermal expansion of the beams. Since these beams are clamped laterally, it will thus deflect in the y-direction. Similar to a heatuator, several chevron devices can be connected in parallel to produce a larger force with limited displacement [72]. Conversely, multi-chevron devices can also be connected in series as illustrated in fig. 24(d). By using insulator beams as the clamped constraint, the device becomes a planar microspring actuator, which is able to deliver a much larger displacement and force [74]. On the other hand, for a bimorph microactuator, its motion is essentially based on the difference in the coefficient of thermal expansion (CTE) between two layers. The difference in CTE will generate an upward (or downward) force, which is able to lift up (or bend down) the active mechanical structure. This is shown schematically in fig. 25. The temperature change can be realized via the ambient temperature or simply through joule heating of a heater resistor. The latter concept typically requires a closed conductive path as part of the bilayer structure.

Most thermal microactuators can be fabricated using surface micromachining technology with a three mask process. Polysilicon has been a popular material for these thermal actuators, largely due to the attractive and mature technology of the MUMPS foundry process [75]. However, it should be noted that metals are generally better than semiconductors

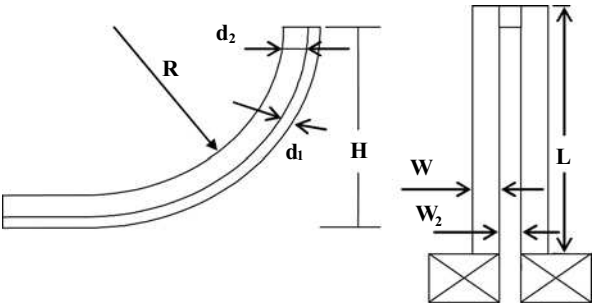

FIGURE 25. A schematic drawing of a bilayer thermal microactuator.

in terms of material choice to fabricate thermal microactuators, largely due to the fact that metals normally have a higher CTE. In fact, metals such as electroplated Ni have recently been accepted as a better material for thermal microactuators due to is higher performance and larger displacements as compared to polysilicon [67]. Due to the flexibility and the versatility of crosslinked PMMA as the sacrificial layer, EBL crosslinked PMMA surface micromachining in combination with Ni electroplating has been employed to fabricate Ni-based thermal microactuators. This fabrication scheme is especially useful for prototyping purposes without incurring a large cost and also useful for laboratories which do not have polysilicon deposition capabilities.

For comparative purposes, fig. 26 shows the schematics for the different process stages involved to fabricate thermal microactuators based on (a) the MUMPS process flow using standard polysilicon surface micromachining and (b) EBL crosslinked PMMA surface micromachining in combination with Ni electroplating. As can be seen from fig. 26, the main process stages for the fabrication of lateral microactuators are bottom electrode formation for a generic process, sacrificial layer formation and the final active layer formation. For the MUMPS process as shown in fig. 26(a), the process flow involved firstly, a thin SiN_x deposition and the 1st layer polysilicon deposition (poly.1) followed by lithography and plasma etch steps to define the polysilicon electrodes. Next, a sacrificial layer such as SiO_2 or PSG is deposited, lithographically patterned and subsequently plasma etched to define the vias that connect the 2nd level polysilicon layer (poly.2) with the poly.1 layer. The poly.2 layer is then deposited and goes through similar patterning processes as before to define the main mechanical layer. Finally, the devices are released by etching away the sacrificial SiO_2 or PSG layer. For the EBL crosslinked surface micromachining process flow as shown in fig. 26(b), which uses crosslinked PMMA as the sacrificial layer, the 1st layer of metal (metal.1) which serves as the contact electrodes is defined via a lift-off process using Au or Al thin films. When the contacts are defined, multiple layers of PMMA layers are spun on, baked at 150°C for 15 mins and finally, EBL crosslinked to selectively define the solid sacrificial layer. For this purpose, a dose of more than 120 C/m^2 at 25 kV is used. By immersing the sample in acetone, patterned crosslinked PMMA sacrificial layers of 0.5 to 1.0 μm in thickness are realized. Next, a seed layer consisting of Cr/Au thin films is deposited on the PMMA sacrificial layer with typical thicknesses ranging between 10 to 20 nm. A conventional optical lithography step follows to form the plating mould. Nickel is then electroplated in a nickel sulphamate bath [33] at an optimal temperature between

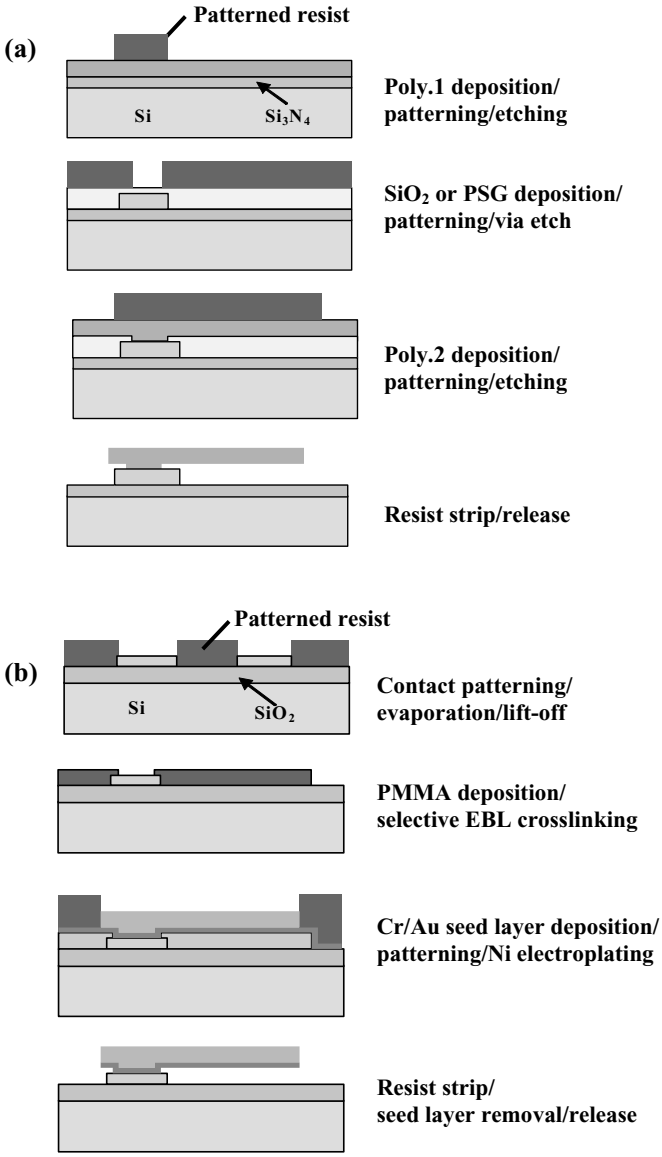

FIGURE 26. Schematics of the thermal microactuator fabrication process based on (a) MUMPS process flow using standard polysilicon surface micromachining and (b) EBL crosslinked PMMA surface micromachining in combination with Ni electroplating.

40 to 60°C and a current density of about 2 mA/cm^2. This is in order to get a low stress active material for the actuator layer. After plating, the photoresist and the seed layer on the outside of the device area are removed by acetone and acid, respectively. The actuators are finally released by etching the PMMA sacrificial layer in oxygen plasma. The technique of patterning electroplated Ni using through-mask plating is widely accepted as a simple

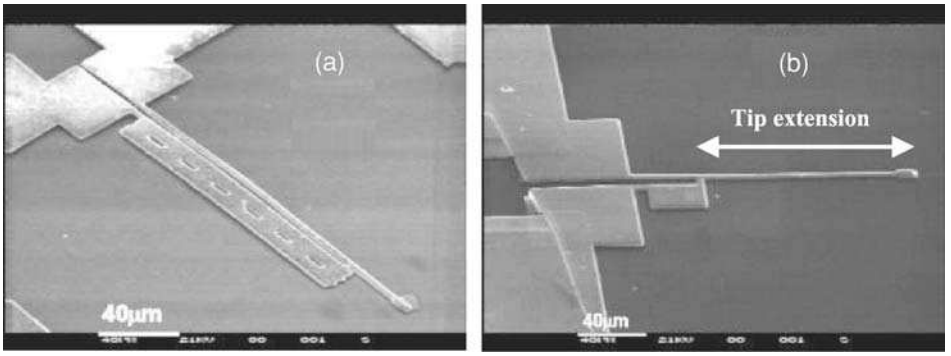

FIGURE 27. SEM micrographs of two different designs of free-standing Ni heatuators based on the EBL crosslinked PMMA surface micromachining process flow.

way to fabricate lateral thermal microactuators. The main advantage of using crosslinked PMMA as the sacrificial layer is due to the simplicity in the process. In other words, no special or expensive deposition system is required for depositing sacrificial material systems such as SiN_x or metals. The crosslinked PMMA sacrificial layer can also be easily removed by an oxygen plasma etch step in a relatively short time. This dry release step helps to avoid potential stiction effects. The possibility of using EBL to pattern both the sacrificial layer and also the active mechanical element affords the fabrication of thermal actuators with submicron dimensions. This would be useful to investigate the scalability of the use of thermal actuation to produce efficient NEMS devices. Depending on application, some of the problems faced when using crosslinked PMMA as the sacrificial layer is the difficulty involved in having a reasonably thick gap between the microactuator and the substrate. This large gap is often necessary to improve the efficiency of the thermally actuated mechanical device by reducing the rate of heat loss from the actuator to the substrate below. Nevertheless, this can be solved by using multiple spun-on PMMA layers. It is worthy of mention that the generic 3-masks (including EBL) MUMPS and PMMA process as shown in fig. 26, are for devices where the contact electrodes are made separately from that of the moving parts. For planar thermal actuators, these processes can be simplified into a 2-masks process with the electrodes and the moving parts realized in a single mask step.

Figure 27 shows SEM micrographs of two different designs of free-standing Ni heatuators based on the EBL crosslinked PMMA surface micromachining process flow. In fig. 27(a), the fabricated heatuator has a hot arm length/width ratio (L_h/W_h) of 120 μm/2 μm and a cold arm length/width ratio (L_c/W_c) of 110 μm/20 μm. In fig. 27(b), the design of the heatuator is such that the hot arm length/width ratio is 40 μm/2 μm while the cold arm length/width ratio is 36 μm/20 μm. Both designs have a gap of 1.5 μm between the hot and cold arms as well as gap of 500 nm between the active mechanical layers and the bottom substrate. The 500 nm gap corresponds to the thickness of the EBL crosslinked PMMA sacrificial layer before release. The heatuator depicted in fig. 27(a) has a longer active hot arm and therefore, can deliver a larger force as compared to the heatuator design shown in fig. 27(b). In addition, the longer hot arm design allows the heatuator to be operated at a lower temperature. As for the heatuator device shown in fig. 27(b), a long beam is used to amplify the displacement induced by the active hot and cold arms, which are smaller

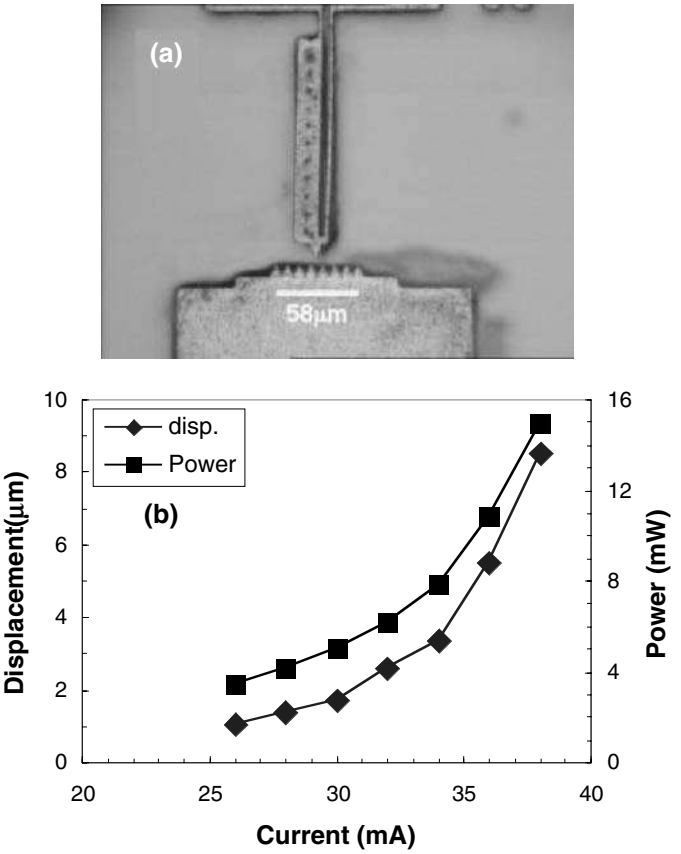

FIGURE 28. (a) An optical micrograph illustrating the in-plane motion of a surface micromachined heatuator when a current of 36 mA was applied and (b) plots of the displacement and the electrical power of the same device as a function of applied current.

in terms of dimensions. The comparatively larger tip at the end of the long arms for the heatuators shown in fig. 27 is designed to facilitate a good and stable contact force so that the heatuators can be used in switching applications.

Figure 28 (a) shows an optical micrograph demonstrating the in-plane motion of a surface micromachined heatuator (with an $L_h/L_g = 160$ μm/20 μm) when a current of 36 mA was applied. This in-plane heatuator was made using a single mask process with Ni layers (which act as the mechanical layers) plated directly onto the SiO_2/Si substrate before being released by SF_6 dry etching [67]. As can be seen, the heatuator shows a large displacement of about 5 μm in the lateral direction. For the purpose of calibrating the actuating process and the amount of power needed, fig. 28(b) plots both the displacement and the electrical power as a function of the current being applied to the device. For these dc measurements, a Keithley 2400 source measure unit (SMU) is used to provide a constant current source with the voltage drop across the device being monitored. The heatuator is mounted on a probe station with a video camera to capture the images, as it deflects.

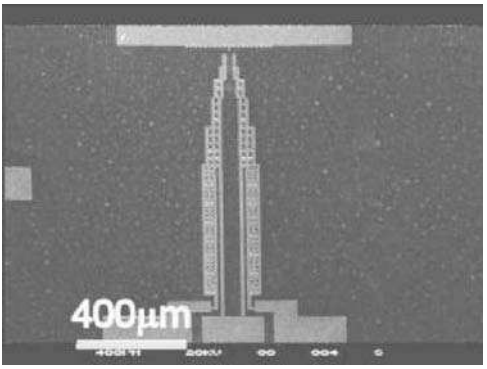

FIGURE 29. An SEM micrograph of a microfabricated set of thermally-actuated tweezers. A set of regularly spaced marks is provided adjacent to the tip to calibrate its displacement.

Typical values of dc current used to actuate the devices are in the range of 20 to 40 mA. The consumed power is then calculated using the measured values of the current and voltage, which includes those consumed by the bond pads and probes. As can be observed from fig. 28(b), the displacement appears to increase with increasing current in a quadratic manner. This is anticipated because the displacement, d of a heatuator is typically proportional to the temperature difference between the cold and the hot arms, and inversely proportional to the flexural rigidity [67]:

$$d \propto \frac{\alpha \Delta T_{ave}}{E} = \frac{\alpha V^2}{k \rho E} \tag{1}$$

where α, ΔT_{ave}, E, V, k and ρ are the CTE, the average temperature difference, the Young's modulus, the applied voltage, the thermal conductivity and the density, respectively. A detailed analysis of heat transfer within a device and the governing equations for its actuation can be found in refs. [76] and [77].

Finally, fig. 29 shows an SEM micrograph of a microfabricated set of tweezers, realized by fabricating two heatuators with the hot arms facing each other. When a current flows from the left arm actuator to the right arm actuator via the outer bond pads, the inner hot arms of both actuators are heated up more than the outer cold arms. This will result in the outward deflection of both heatuators and will allow the tip of the microtweezers to open. When the current flow stops, the actuators will return to the original positions. This form of mechanism enables the spatial micromanipulation of small objects with good precision. The dimensions of the devices shown in fig. 29 include: L_h/W_h ratio of 600 µm/4 µm with a tip extension of 400 µm and L_c/W_c ratio of 550 µm/36 µm. Typical current values needed for the actuation of the microtweezer is between 40 to 60 mA with a power consumption of about 30 mW.

In summary, microelectrothermal actuator is an important class of devices for MEMS and NEMS. These devices have the advantage of delivering large forces and large displacements, which are typically limited when electrostatic based actuation is used. Also, they have the flexibility of being operated in both voltage and current modes. The fabrication process for thermal microactuators is relatively straight forward and simple as compared to other more complicated MEMS/NEMS devices. In fact, with proper design, a single mask

process is even possible. On this note, the EBL crosslinked PMMA sacrificial material system will find applications in fabricating these thermal microactuators. This is by serving as both the low-dimensional sacrificial layer and also as the electroplating mould for forming the metallic active mechanical elements. The capability of using EBL to pattern the sacrificial layer and the mechanical layer is advantageous in terms of extending the critical size of these devices into the NEMS domain. However, one should be aware that thermal microactuators typically suffer from a high operating temperature and also large power consumption. Therefore, a proper material choice for the mechanical element is important to allow good functionality and reliability. When successful, microelectrothermal actuators are particularly useful for biological and biomedical applications where activities such as cell isolation, probing and measurements are commonly performed. This is because electrostatic actuators are normally ineffective in salty water while piezoelectric devices require a large voltage.

4. SELECT FUNDAMENTAL RESEARCH

Advancing technologies in EBL and molecular beam epitaxy (MBE) have made it possible to prepare high-quality and high-resolution nanostructures for fundamental physics research. By patterning the nanostructures to submicrometer dimensions coupled with electrostatic squeezing techniques [78] where necessary, a small number of electrons, down to the single-electron limit can be isolated and their effective dimensionality varied. This allows for the progressive development of nanostructure physics, which is part of the growing field of mesoscopic physics and nanoelectronics in general. For example, by patterning Schottky gates over a high-quality GaAs/AlGaAs heterostructure, electrostatically-defined nanostructures such as one-dimensional (1-D) constriction [78], quantum antidots [30], quantum dots [79] and a large variety of related quantum devices can be experimentally realized.

A key to the success of the EBL technique is the ability to pattern nanostructures in an appropriate resist. In most cases, PMMA resist is used as the polymeric media for EBL in the form of a high-resolution positive resist. As a positive resist, the regions exposed to the electron beam (with conventional dose) are subsequently removed after development in a suitable solvent such as the 3 IPA: 1 MIBK developer. In this regard, PMMA has been proven to be a very reliable positive resist for EBL over the past years giving readily achievable line widths of several nanometers. However, for some low-dimensional physics experiments, a negative resist with good dielectric properties, which becomes insoluble in the developer after exposure, is also required. Most negative resists suffer from problems which include: having a low patterning resolution, swelling during the development step, uncontrolled cracking during cool-down to low temperatures (which is necessary to avoid thermal smearing for the observation of quantum features), or possessing a high degree of sensitivity to the processing parameters [30]. In addition, some negative resists require coating by means of sputtering or even evaporation, which may add on to the complexity of the process and may even affect the quality of the defined electron system. Therefore, a reliable high-resolution negative resist, which can be easily deposited by spin coating while offering good dielectric properties, is highly desirable for the fabrication of multilayered gated quantum devices. The ability to use PMMA as both a positive and negative resist by modulating the received amount of electron dose provides a simple and flexible method

for high resolution patterning of an insulating layer (in the form of crosslinked PMMA). The fact that crosslinked PMMA is resistant to most solvents including acetone, greatly simplifies the fabrication of quantum devices consisting of interdigitating (both adjacent and on top of one another) conducting and insulating layers. This processing capability helps to realize the fabrication of multilayer gated quantum devices, which will be briefly discussed in the next subsection.

4.1. Nanofabrication of Multilayered Gated Quantum Devices

Using PMMA as both negative and positive resists in the same fabrication process, Zailer and co-workers [30] have successfully demonstrated that it is possible to fabricate complex multilayer semiconductor nanostructures for low-dimensional physics experiments. Figs. 30(a)–(h) show the generic process flow for fabricating a quantum nanostructure consisting of a dot gate in the middle of a split-gate device with a second layer of metallization [30] at the top using the positive/negative PMMA approach. Here, crosslinked PMMA resist is used as an insulator to facilitate the contacting of the dot gate in the middle of the split-gate device. Fig. 30(a) shows a split-gate structure patterned using standard EBL, metallization and lift-of techniques. PMMA is then spun on and exposed in the required regions [see fig. 30(b)]. In fig. 30(c), the PMMA resist is exposed in the middle of the split-gate gap and was subsequently developed, leaving a tiny hole behind. Next, the PMMA layer is selectively crosslinked by high dose EBL to form thin insulating layers near each pair of the split-gate structures [see fig. 30(d)]. After crosslinking, the sample is then immersed in acetone to remove the unexposed regions of the PMMA resist [see fig. 30(e)]. A new layer of PMMA is then spun on [see fig. 30(f)] and exposed in the regions where the required top metallization is to be deposited. After developing [see fig. 30(g)], the device is finally metallised in a lift-off process to produce the desired device [see fig. 30(h)] structure. Fig. 30(i) shows an SEM micrograph of four split-gate devices fabricated on a high-mobility GaAs/AlGaAs heterostructure with a second layer of gate metallization deposited on top to contact the central dots (via the holes in the crosslinked PMMA). The dark rectangle around the four split-gate structures is the crosslinked PMMA. To enable control of the dot gates, a top metallization in the form of a horizontal bar is used to connect all four dots, over the crosslinked PMMA, to one of the side gates [30]. It is also possible to fabricate an independent contact for each of the dots. The quantum device shown in fig. 30(i) demonstrates the possibility of patterning submicrometer features on top of thin layers of crosslinked PMMA layer (down to 25 nm) [30]. More importantly, the crosslinked PMMA layer acts as a good and uniform dielectric layer (even at such thicknesses) so that the dot gate and the split-gate can be independently controlled. The device shown in fig. 30(i) is measured in a dilution refrigerator with the results shown in fig. 30(j). By sweeping the magnetic field, or the dot-gate bias, single-particle states around the dot-gate can be detected in the form of Aharnov-Bohm oscillations [see fig. 30(j)]. The versatile design of the device using crosslinked PMMA as the dielectric layer is indispensable for observing large-amplitude Aharonov-Bohm oscillations, as shown in fig. 30(j), both in the integer and the fractional quantum Hall regime. The measured period of oscillations is about 17 mT, which corresponds to a dot diameter of about 500 nm. The ability to observe such oscillations demonstrates that the high dose exposure required to crosslink the PMMA resist does not degrade the heterojunction transport characteristics appreciably.

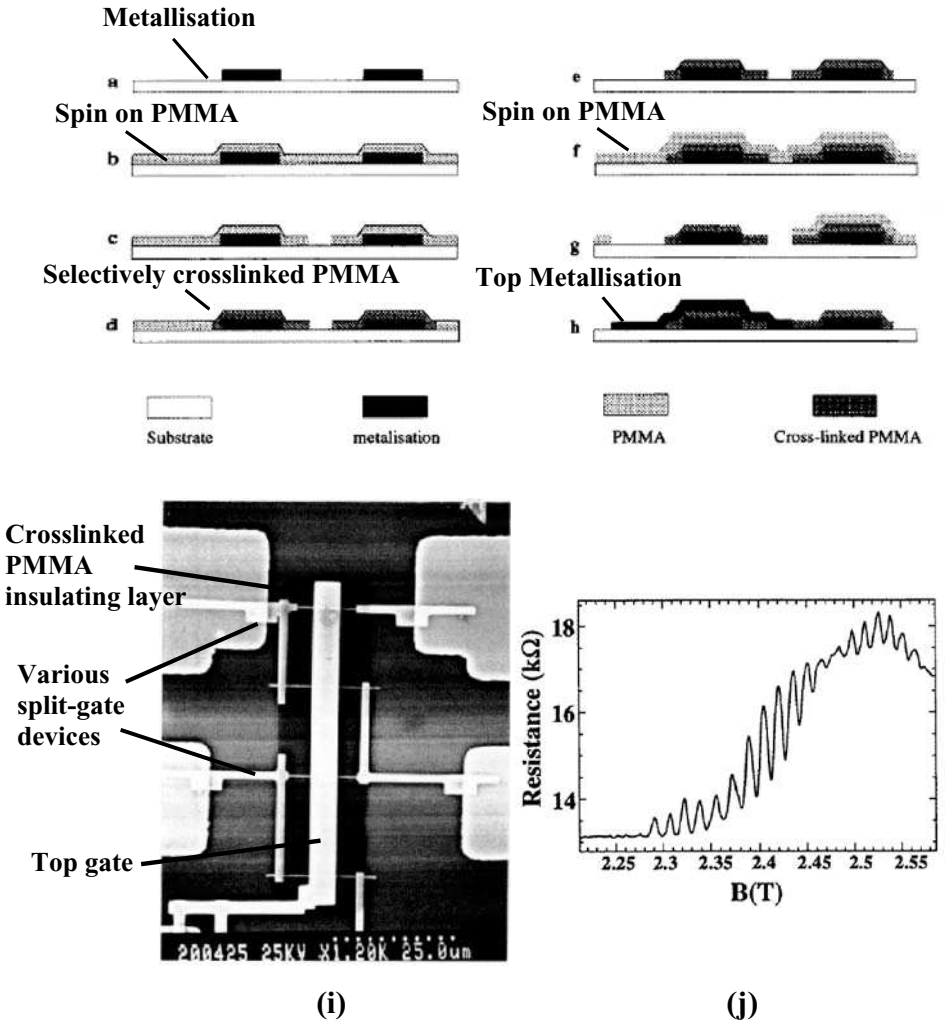

FIGURE 30. (a)–(h): A generic process flow for fabricating quantum nanostructures using the positive/negative PMMA approach. (i) An SEM micrograph of a multilayered quantum device consisting of four split-gate structures with a top gate connecting to the central dot gate via the holes in the crosslinked PMMA resist. (j) Aharonov-Bohm oscillations measured using the device at dilution refrigerator temperatures. (Adapted from I Zailer *et. al.* (1996) *Semicond. Sci. Technol.*, **11**, 1235–1238. © 1996 IOP Publishing Ltd. With permission.)

A 1-D ballistic constriction has been attracting a great deal of interest. In such a system, it is possible to observe conductance quantization at zero magnetic field. Using crosslinked PMMA as a gate dielectric, Liang and co-workers have fabricated a clean 1-D channel in which the potential profile within the 1-D channel can be varied [80]. The device consists of a two-layered Schottky gate patterned by EBL on the surface of a high mobility GaAs/$Al_{0.33}Ga_{0.67}As$ heterostructure, 157 nm above the defined two-dimensional electron gas (2DEG). Acting as a thin dielectric layer between the split-gate structures and

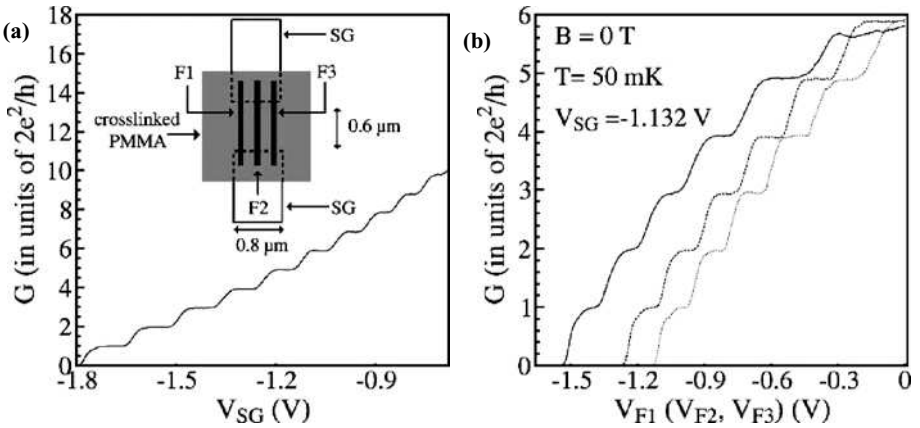

FIGURE 31. (a) Conductance measurements $G(V_{SG})$ as a function of split-gate voltage V_{SG} for all finger gates at 0 V. The inset shows a schematic device diagram. There are three finger gates labeled as F1, F2, and F3 lying above the split-gate (SG), with an insulating layer of crosslinked PMMA in between. (b) $G(V_{F1})$ (in solid line), $G(V_{F3})$ (in dashed line), $G(V_{F2})$ (in dotted line) for $V_{SG} = -1.132$ V when each one of the finger gates is swept while the others are grounded to the 2DEG. (From C.-T. Liang *et. al.* (2001) *Jpn. J. Appl. Phys.*, **40**, 1936–1940. © 2001 The Japan Society of Applied Physics. With permission.)

gating fingers, a 30 nm thick crosslinked PMMA, which has been highly dosed by EBL, is used. The thin insulating layer of crosslinked PMMA allows the independent control of all the gates. The transport properties of the 2DEG are such that the mean free path (16.5 μm) is much longer than the effective 1-D channel length. Measurements of the two-terminal conductance G are performed at 50 mK with standard phase-sensitive techniques. The results of conductance measurements $G(V_{SG})$ as a function of split-gate voltage V_{SG} when all finger gate voltages V_{F1}, V_{F2}, and V_{F3} are zero is shown in fig. 31(a). Here, conductance plateaus at multiples of $2e^2/h$, with no resonant feature superimposed on top, can be found (which is anticipated for a clean 1-D channel). In addition, when the channel is defined at $V_{SG} = -1.132$ V, five quantized conductance steps are noticed when each of the finger gates is swept with the rest grounded to the 2DEG, as shown in fig. 31(b). These experiment results demonstrate that a clean 1-D channel is formed where impurity scattering is negligible. More importantly, from a processing point of view, the presence of the crosslinked PMMA, together with the three overlaying finger gates, does not affect the flatness and clarity of the 1-D ballistic conductance steps. The results also reveal the excellent dielectric properties of low-dimensional crosslinked PMMA and its usefulness in fabricating quantum devices.

A zero-dimensional (0-D) quantum dot [81], which can be considered as a puddle of electrons, has been attracting a great deal of experimental and theoretical interest. A firm understanding of the surrounding physics will lead to potential applications such as the development of the single-electron transistor (SET) and ultimately, the possible realization of a solid-state based quantum information system. The developed technique of nanomachining submicrometer features in crosslinked PMMA using EBL also allows simple, yet unique fabrication of multilayer quantum devices [17, 82]. By using crosslinked PMMA as an insulating dielectric layer, the negative/positive PMMA technique was used to fabricate

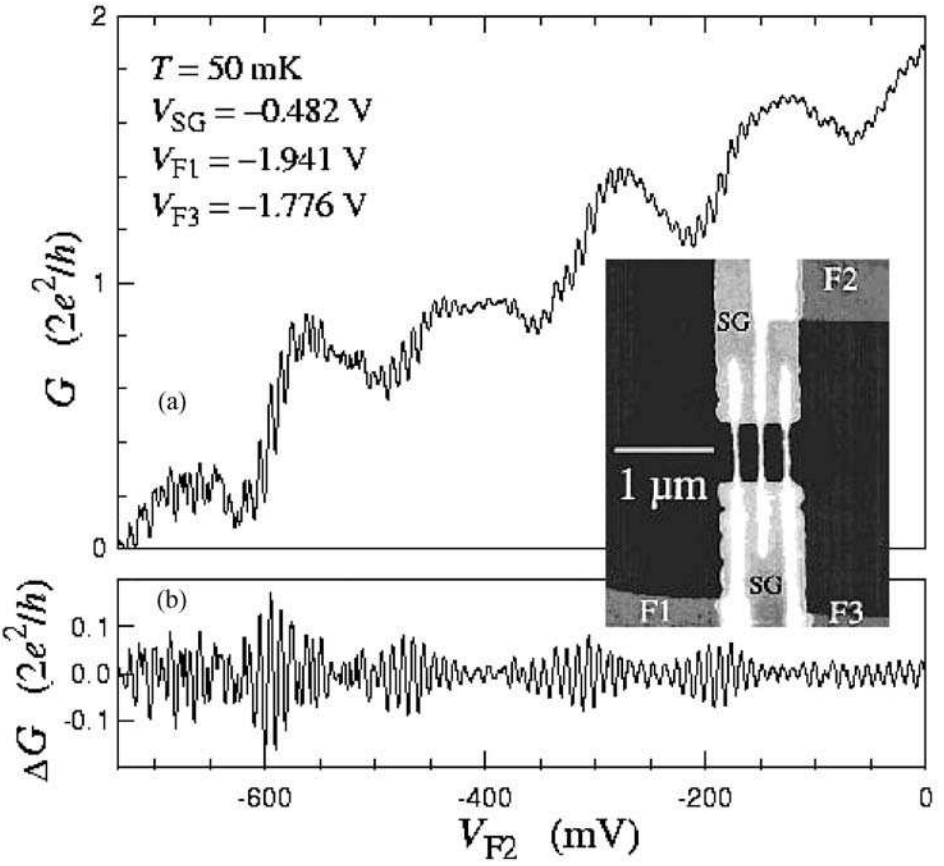

FIGURE 32. (a) Conductance measurements $G(V_{F2})$ for $V_{SG} = -0.482$ V, $V_{F1} = -1.941$ V and $V_{F3} = -1.776$ V. (b) The oscillations without the background which shows the beating pattern. The inset shows a SEM picture of a typical device. The brightest regions correspond to finger gates with joining pads, lying above the split-gate (SG), with an insulating layer of crosslinked PMMA in between. (From W.H. Teh *et. al.* (2003) *IEEE/ASME J. Microelectromech. Syst.*, **12**, 641–648. © 2003 IEEE. With permission.)

multilayered gated lateral quantum dot devices [see inset of fig. 32] [17]. There are three major steps in this fabrication technique. First, a split-gate device is made on a Hall bar using standard EBL. Second, PMMA resist is spun on the Hall bar at 8000 rpm for 40 s, which results in a 70 nm thick PMMA layer. The solution-coated sample is subsequently baked at 150°C for 15 mins. The central regions near the split-gate are heavily exposed by an electron beam, which gives a dose of 120 C/m^2. In this case, there is a layer of crosslinked PMMA that can be used as a gate dielectric. Finally, three overlaying finger gates with joining pads are aligned and fabricated above the split-gate device. The inset to fig. 32 shows the SEM picture of a typical device. The existence of the crosslinked PMMA acting as a dielectric allows the independent control of all the gates. By negatively biasing the split-gate (SG), and the finger gates F1 and F3, an electrostatically-defined lateral quantum dot device can be experimentally realized. As can be seen in fig. 32, there are two sets of oscillations, which

confirm the reliability of the insulating properties of crosslinked PMMA at low temperatures, down to 50 mK. When the applied voltage on the second finger gate (F2) is varied, periodic and continuous oscillations superimposed on resonant feature can be observed, as shown in fig. 32(a). Decreasing V_{F2} has two effects. First, it reduces the number of electrons in the quantum dot, causing continuous conductance oscillations due to Coulomb blockade effects. Second, it reduces the number of transmitted 1-D channels through the dot. The latter effect gives rise to the slowly varying background Fabry-Perot type resonant effects: constructive and destructive interference near the entrance and exit to the channel [83]. Fig. 32(b) shows the beating pattern after subtraction of the background. Here, it is worth mentioning that the fast oscillations for $G > 2e^2/h$, which correspond to Coulomb charging effects in an open quantum dot at zero magnetic field [82, 84] challenges our conventional understanding of charging. Therefore, the use of crosslinked PMMA allows this completely new physical effect to be observed and experimented.

In summary, it has been shown that a layer of crosslinked PMMA can be used as a gate dielectric for multilayered gated structures, allowing new physical phenomena, such as Coulomb charging effects in an open system at zero magnetic field to be observed. Fabrication technologies and physics often go hand in hand. Advances in technology make it possible to prepare higher-quality, better devices which could lead to observations of new effects in physics. A thorough understanding of underlying physics will result in the progress and improvement in technology. The use of crosslinked PMMA can greatly simplify the fabrication process for multilayer nanostructures, which allow us to investigate unexpected physical effects, such as Coulomb charging in an open dot and also, Kondo-like effects in a quantum antidot. With crosslinked PMMA as a reliable and useful material in basic research and MEMS, it is highly likely that novel mechanical quantum devices can be realized in the near future.

5. CONCLUSIONS

Crosslinked PMMA as a sacrificial material for surface nanomachining using EBL has been investigated and characterized. Crosslinked PMMA can be used for the quasi 3-D fabrication of sacrificial layers in the nanometer scale using EBL in a single process step. The crosslinked PMMA sacrificial layer is easy to coat, simple to fabricate, easy to dissolve by dry-etching, offers direct high resolution EBL patterning, flexible, compatible with different metallic materials, possesses good dielectric properties and offers low temperature post-processing of MEMS/NEMS. It also offers quick turnaround development for MEMS/NEMS devices and is easily accessible to universities and small companies. Freestanding and low stress microstructures such as suspended membranes, paddles, bridges and cantilevers are successfully released over a submicrometer gap using this technique. These structures ultimately lead to unique MEMS/NEMS devices and innovative processing schemes. For the former, examples include the fabrication of electrostatically driven Ni micromechanical tunneling switch and various electro-thermal microactuators. As for the latter, an integration scheme concerning the selected patterning of carbon nanotubes on suspended micro/nanomechanical structures has been introduced. The ability to quasi 3-D surface nanomachine submicrometer features together with the excellent dielectric properties of crosslinked PMMA, are also useful in investigating low-dimensional physics. This,

integrated alongside with NEMS will potentially create novel mechanical quantum devices in the future.

6. ACKNOWLEDGEMENTS

W.H. Teh thanks previous collaborators: K.B.K. Teo, R.G. Lacerda, G.A.J. Amarantunga and W.I. Milne of the Engineering Department, Cambridge University for growing the carbon nanotubes; M. Castignolles and A. Loiseau of the Laboratoire d'Etude des Microstructures (LEM), France for the TEM's and M.R. Graham of Cambridge University for useful technical discussions. W.H. Teh acknowledges support from Cavendish Kinetics Ltd and Ph.D. scholarship support from NSTB/IME.

J.K. Luo thanks W.I. Milne of Cambridge University and S.M. Spearing of M.I.T. for useful technical discussions and support. The research on thermal microactuators is partially supported by the Cambridge-M.I.T. Institute under grant number 059/P.

C.T.L thanks the UK EPSRC for funding the work on quantum nanostructures. He acknowledges D.G. Baksheyev, C.H.W. Barnes, C.J.B. Ford, J.D.F. Franklin, J.E.F. Frost, A.R. Hamilton, M. Pepper, M.Y. Simmons, D.A. Ritchie, V.I. Talyanskii, O.A. Tkachenko and V.A. Tkachenko for helpful discussions. He acknowledges financial support from the NSC, Taiwan (NSC 89-2911-I-002-104 and 42006F), the Department of Physics of National Taiwan University and the Royal Society, UK.

C.G. Smith thanks the UK EPSRC and Cavendish Kinetics Ltd. for supporting the work on MEMS/NEMS and quantum nanostructures.

REFERENCES

1. Michael Roukes, Nanoelectromechanical Systems Face the Future, *Physics World*, Feb. 2001;25–31.
2. Michael Roukes, Plenty of Room, Indeed, *Scientific American*, Sept. 2001;48–57.
3. Craighead, H.G., Nanoelectromechanical Systems, *Science*, 2000;290:1532–1535.
4. Bean, K.E., Anisotropic Etching of Silicon, *IEEE Trans. Electron Devices*, 1978;ED-25(10):1185–1193.
5. Bassous, E., Fabrication of Novel Three-dimensional Microstructures by the Anisotropic Etching of (100) and (110) Silicon, *IEEE Trans. Electron Devices*, 1978;ED-25(10):1178–1185, .
6. Nathanson, H.C. and Wickstrom, R.A., A Resonant Gate Transistor with High-Q Bandpass Properties, *Appl. Phys. Lett.*, 1965;7:84–86.
7. Gardner, J.W., Varadan, V.K., and Awadelkarim, O.O., *Microsensors, MEMS and Smart Devices*. Chichester, UK: John Wiley & Sons, 2001.
8. Howe, R.T. and Muller, R.S., Polycrystalline Silicon Micromechanical Beams, in *Spring Meeting of the Electrochemical Society*, Montreal, Canada, 1982, pp. 184–185.
9. Guckel, H. and Burns, D.W., A Technology for Integrated Transducers, in *Int. Conf. on Solid-state Sensors and Actuators*, Philadelphia, PA, USA, 1985, pp. 90–92.
10. Howe, R.T., Surface Micromachining for Microsensors and Microactuators, *J. Vac. Sci. Technol. B*, 1988;6(6):1809–1813.
11. Schmidt, M.A., Howe, R.T., Senturia, S.D., and Haritonidis, J.H., Design and Calibration of a Microfabricated Floating-element Shear-stress Sensor, *IEEE Trans. Electron Devices*, 1988;35:750–757.
12. Löchel, B., Maciossek, A., Knig, M., Quenzer, H.J., and Huber, H.-L., Galvanoplated 3D Structures for Micro Systems, *Microelectron. Eng.*, 1994;23:455–459.
13. Paul M. Zavracky, Sumit Majumder, and Nicol E. McGruer, Micromechanical Switches Fabricated Using Nickel Surface Micromachining, *J. Microelectromech. Syst.*, 1997;6(1):3–9.

14. Burbaum, C., Mohr, J., and Bley, P., Fabrication of Capacitive Acceleration Sensors by the LIGA Technique, *Sensors Actuators A*, 1991;27:559–563.
15. Frazier, A.B., Ahn, C.H., and Allen, M.G., Development of Micromachined Devices Using Polyimide-based Processes, *Sensors Actuators A*, 1994;45:47–55.
16. Maciossek, A., Löchel, B., Quenzer, H., Wagner, B., Shulze, S., and Noetzel, J., Galvanoplating and Sacrificial Layers for Surface Micromachining, *Microelectron. Eng.*, 1995;27:503–508.
17. Teh, W.H., Liang, C.-T., Graham M.R., and Smith, C.G., Crosslinked PMMA as a Low-dimensional Dielectric Sacrificial Layer, *IEEE/ASME J. Microelectromech. Syst.*, 2003;12(5):641–648.
18. Teh, W.H. and Smith, C.G., Fabrication of Quasi-three-dimensional Micro/Nanomechanical Components Using Electron Beam Cross-linked Poly (Methyl Methacrylate) Resist, *J. Vac. Sci. Technol. B*, 2003;21(6):3007–3011.
19. Zheng Cui, and Ron A Lawes, A New Sacrificial Layer Process for the Fabrication of Micromechanical Systems, *J. Micromech. Microeng.*, 1997;7:128–130.
20. Bartek, M. and Wolffenbuttel, R.F., Dry Release of Metal Structures in Oxygen Plasma: Process Characterization and Optimization, *J. Micromech. Microeng.*, 1998;8:91–94.
21. Bagolini, A., Pakula, L., Scholtes, T.L.M., Pham, H.T.M., French, P.J., and Sarro, P.M., Polyimide Sacrificial Layer and Novel Materials for Post-processing Surface Micromachining, *J. Micromech. Microeng.*, 2002;12:385–389.
22. Monk, M. and Gale, R.O., The Digital Micromirror Device for Projection Display, *Microelectronic Engineering*, 1995;27:489–493.
23. Hyuk-Jeen Suh, Pamidighantam Bharathi, David J. Beebe, and Jeffrey S. Moore, Dendritic Material as a Dry-release Sacrificial Layer, *J. Microelectromech. Syst.*, 2000;9(2):198–205.
24. Bernstein, G.H., Goodson, H.V., and Siner, G.L., Fabrication Technologies for Nanoelectromechanical Systems, in Mohamed Gad-el-Hak (Ed.), *The MEMS Handbook*, London, UK: CRC Press, 2002, pp. 36–1.
25. McCord, M.A. and Rook, M.J., Electron Beam Lithography, in P. Rai-Choudhury (Ed.), *Handbook of Microlithography, Micromachining, and Microfabrication*: *Microlithography*, Bellingham, WA: SPIE Press, 1997, Vol. 1, pp. 139–250.
26. Hasko, D.G., Yasin, S., and Mumtaz, A., Influence of Developer and Development Conditions on the Behavior of High Molecular Weight Electron Beam Resists, *J. Vac. Sci. Technol. B*, 2000;18(6):3441–3444.
27. Harris, R.A., Polymethyl Methacrylate as an Electron Sensitive Resist, *J. Electrochem. Soc. Solid-State Sci. Technol.*, 1973;120:270–274.
28. James S. Greeneich, Developer Characteristics of Poly-(Methyl Methacrylate) Electron Resist, *J. Electrochem Soc.*, 1975;122:970–976.
29. Tada, T. and Kanayama, T., Fabrication of Silicon Nanostructures with a Poly(methylmethacrylate) Single-Layer Process, *J. Vac. Sci. Technol. B*, 1995;13:2801–2804.
30. Zailer, I., Frost, J.E.F, Chabasseur-Molyneux, V., Ford, C.J.B., and Pepper, M., Crosslinked PMMA as a High-resolution Negative Resist for Electron Beam Lithography and Applications for Physics of Low-dimensional Structures, *Semicond. Sci. Technol.*, 1996;11:1235–1238.
31. Kley, E.-B., Continuous Profile Writing by Electron and Optical Lithography, *Microelectron. Eng.*, 1997;34:261–298.
32. Teh, W.H., *Physics and Fabrication of Metallic Micro/Nanoelectromechanical Devices and 3-D Photoplastic Structures*, Ph.D. dissertation, University of Cambridge, UK, 2003.
33. Teh, W.H., Luo, J.K., Graham, M.R., Pavlov, A., and Smith, C.G., Near-zero Curvature Fabrication of Miniaturized Micromechanical Ni Switches Using Electron Beam Cross-linked PMMA, *J. Micromech. Microeng.*, 2003;13:591–598.
34. Teh, W.H., Luo, J.K., Graham, M.R., Pavlov, A., and Smith, C.G., Switching Characteristics of Electrostatically Actuated Miniaturized Micromechanical Metallic Cantilevers, *J. Vac. Sci. Technol. B*, 2003;21(6):2360–2367.
35. Teh, W.H. and Smith, C.G., Reversible Electrostatic Control of Micro-mechanical Structure Tunneling Characteristics, *J. Appl. Phys.*, 2003;94(7):4614–4618.
36. Teh, W.H., Smith, C.G., Teo, K.B.K., Lacerda, R.G., Amaratunga, G.A.J., Milne, W.I., Castignolles, M., and Loiseau, A., Uniform Patterned Synthesis of Vertically-Aligned Carbon Nanotubes on Low-Stress Micromechanical Structures, in *Proceeding of the 12th International Conference on Solid-State Sensors, Actuators and Microsystems (Transducers 2003)*, Boston, MA, USA, 2003, Vol. 1, pp. 190–193.
37. Teh, W.H., Smith, C.G., Teo, K.B.K., Lacerda, R.G., Amaratunga, G.A.J., Milne, W.I., Castignolles, M., and Loiseau, A., Integrating Vertically Aligned Carbon Nanotubes on Micromechanical Structures, *J. Vac. Sci. Technol. B*, 2003;21(4):1380–1383.

38. Smith, C.G., Ahmed, H., Kelly, M.J., and Wybourne, M.N., The Physics and Fabrication of Ultra-Thin Free-Standing Wires, *Superlattices and Microstructures*, 1985;1:153–154.
39. Smith, C.G. and Wybourne, M.N., Electric-Field Heating of Supported and Free-Standing AuPd Fine Wires, *Solid State Commun.*, 1986;57:411–416.
40. Hasko, D.G., Potts, A., Cleaver, J.R.A., Smith, C.G., and Ahmed, H., Fabrication of Submicrometer Free-Standing Single-Crystal Gallium Arsenide and Silicon Structures for Quantum Transport Studies, *J. Vac. Sci. Technol. B*, 1988;6:1849–1851.
41. Hasko, D.G., Smith, C.G., Lucek, J.K., Cleaver, J.R.A., and Ahmed, H., Fabrication and Electrical, Mechanical and Thermal Properties of Sub-micron Free-Standing Devices, *Microelectron. Eng.*, 1989;9:337–340.
42. Schwab, K., Henriksen, E.A., Worlock, J.M., and Roukes, M.L., Measurement of the Quantum of Thermal Conductance, *Nature*, 2000;404:974–977.
43. Chan, H.B., Aksyuk, V.A., Kleiman, R.N., Bishop, D.J., and Capasso, Federico, Quantum Mechanical Actuation of Microelectromechanical Systems by the Casimir Force, *Science*, 2001;291:1941–1944.
44. Hammel, P.C., Zhang, Z., Moore, G.J., and Roukes, M.L., Subsurface Imaging with the Magnetic Resonance Force Microscope, *J. Low Temp. Phys.*, 1995;101:59–69.
45. Cleland, A.N. and Roukes, M.L., A Nanometer-Scale Mechanical Electrometer, *Nature*, 1998;392:160–162.
46. Petersen, K.E., Micromechanical Membrane Switches on Silicon, *IBM Journal of Research and Development*, 1978;23(4):376–385.
47. Grétillat, M.-A., Thiébaud, P., Linder, C., and de Rooij, N.F., Integrated Circuit Compatible Electrostatic Polysilicon Microrelays, *Journal of Microelectronics and Microengineering*, 1995;5(2):156–160.
48. Majumder, S., McGruer, N.E., and Zavracky, P.M., Electrostatically Actuated Micromechanical Switches, *J. Vac. Sci. Technol. A*, 1997;15:1246–1249.
49. Yao, J.J. and Chang, M.F., A Surface Micromachined Miniature Switch for Telecommunications Applications with Signal Frequencies from DC up to 4GHz, in *Digest of Technical Papers, Transducers 1995*, Stockholm, Sweden, 1995;2:384–387.
50. Randall, J.N., Goldsmith, C., Denniston, D., and Lin, T.-H., Fabrication of Micromechanical Switches for Routing Radio Frequency Signals, *J. Vac. Sci. Technol. B*, 1996;14(4):3692–3696.
51. Goldsmith, C., Lin, T.-H., Powers, B., Wu, W.-R., and Norvell, B., Micromechanical Membrane Switches for Microwave applications, in *Proceeding of the 1995 IEEE MTT-S International Microwave Symposium*, Orlando, FL, 1995, Vol. 1, pp. 91–94.
52. Ami Chand, Mario B. Viani, Tilman E. Schäffer, and Paul K. Hansma, Microfabricated Small Metal Cantilevers with Silicon Tip for Atomic Force Microscopy, *IEEE/ASME J. Microelectromech. Systems*, 2000;9:112–116.
53. Mario B. Viani, Tilman E. Schäffer, Ami Chand, Matthias Rief, Herman E. Gaub, and Paul K. Hansma, Small Cantilevers for Force Spectroscopy of Single Molecules, *J. Appl. Phys.*, 1999;86:2258–2262.
54. Schiele, I., Huber, J., Hillerich, B., and Kozlowski, F., Suface-micromachined Electrostatic Microrelay, *Sensors Actuators A*, 1998;66:345–354.
55. Chen, E.Y., Whig, R., Slaughter, J.M., Cronk, D., Goggin, J., Steiner, G., and Tehrani, S., Comparison of Oxidation Methods for Magnetic Tunnel Junction Material, *J. Appl. Phys.*, 2000;87:6061–6063.
56. Simmons, J.G., Generalized Formula for the Electric Tunnel Effect between Similar Electrodes Separated by a Thin Insulating Film, *J. Appl. Phys.*, 1963;34:1793–1803.
57. Williams, P.A., Papadakis, S.J., Falvo, M.R., Patel, A.M., Sinclair, M., Seeger, A., Helser, A., Taylor II, R.M., Washburn, S., and Superfine, R., Controlled Placement of an Individual Carbon Nanotube onto a Microelectromechanical Structure, *Appl. Phys. Lett.*, 2002;80(14):2574–2576.
58. Ren, Z.F., Huang, Z.P., Xu, J.W., Wang, J.H., Bush, P., Siegal, M.P., and Provencio, P.N., Synthesis of Large Arrays of Well-Aligned Carbon Nanotubes on Glass, *Science*, 1998;282:1105–1107.
59. Teo, K.B.K., Lee, S.B., Chhowalla, M., Hasko, D.G., Ahmed, H., Amaratunga, G.A.J., Milne, W.I., Semet, V., Binh, V.T., Groening, O., Castignolles, M., Loiseau, A., Legagneux, P., Pirio, G., and Pribat, D., Plasma Enhanced Chemical Vapour Deposition Carbon Nanotubes/Nanofibres—How Uniform do they Grow?, *Nanotechnology*, 2003;14:204–211.
60. Franklin, N.R., Wang, Q., Tombler, T.W., Javey, A., Shim, M., and Dai, H., Integration of Suspended Carbon Nanotube Arrays into Electronic Devices and Electromechanical Systems, *Appl. Phys. Lett.*, 2002;81(5):913–915.
61. Yenilmez, E., Wang, Q., Chen, R.J., Wang, D., and Dai, H., Wafer Scale Production of Carbon Nanotube Scanning Probe Tips for Atomic Force Microscopy, *Appl. Phys. Lett.*, 2002;80(12):2225–2227.

62. Bower, C., Zhu, W., Shalom, D., Lopez, D., Chen, L.H., Gammel, P.L., and Jin, S., On-chip Vacuum Microtriode Using Carbon Nanotube Field Emitters, *Appl. Phys. Lett.*, 2002;80(20):3820–3822.
63. Williams, P.A., Papadakis, S.J., Patel, A.M., Falvo, M.R., Washburn, S., and Superfine, R., Fabrication of Nanometer-scale Mechanical Devices Incorporating Individual Multiwalled Carbon Nanotubes as Torsional Springs, *Appl. Phys. Lett.*, 2003;82(5):805–807.
64. Chhowalla, M., Teo, K.B.K., Ducati, C., Rupesinghe, N.L., Amaratunga, G.A.J., Ferrari, A.C., Roy, D., Robertson, J., and Milne, W.I., Growth Process Conditions of Vertically Aligned Carbon Nanotubes Using Plasma Enhanced Chemical Vapor Deposition, *J. Appl. Phys.*, 2001;90(10):5308–5317.
65. Hoffmann, M., Kopka, P., Groβ, T., and Voges, E., Optical Fibre Switches Based on Full Wafer Silicon Micromachining, *J. Micromech. Microeng.*, 1999;9:151–155.
66. Cowan, W.D. and Bright, V.M., Vertical Thermal Actuators for Micro-opto-electro-mechanical Systems, *Proc. SPIE*, 1997;3226:137–146.
67. Luo, J.K., He, J.H., Moore, D.F., Flewitt, A.J., Spearing, S.M., Fleck, N.A., and Milne, W.I., Development of All-metal Electrothermal Actuator and Its Applications, *Proc. SPIE*, 2004;5344:201–210.
68. Chan, H.-Y. and Li, W.J., A Thermally Actuated Polymer Micro Robotic Gripper for Manipulation of Biological Cells, in *Proc. 2003 IEEE Int. Conf. on Robotics & Automation*, Taipei, Taiwan, 2003, pp. 288–293.
69. Ataka, M., Omodaka, A., Takeshima, N., and Fujita, H., Fabrication and Operation of Polyimide Bimorph Actuators for a Ciliary Motion System, *IEEE/ASME J. Microelectromech. Syst.*, 1993;2:146–150.
70. Hickey, R., Kujath, M., and Hubbard, T., Heat Transfer Analysis and Optimisation of Two-beam Microelectromechanical Thermal Actuators, *J. Vac. Sci. Technol. A*, 2002;20:971–974.
71. Moulton, T. and Ananthasuresh, G.K., Micromechanical Devices with Embedded Electro-thermal-compliant Actuation, *Sens. Actuators A*, 2001;90:38–48.
72. Lai, Y.J., McDonald, J., Kujath, M., and Hubbard, T., Force, Deflection and Power Measurements of Toggled Microthermal Actuators, *J. Micromech. Microeng.*, 2004;14:49–56.
73. Luo, J.K., Flewitt, A.J., Spearing, S.M., Fleck, N.A. and Milne, W.I., Modelling of Microspring Thermal Actuator, in *Proc. of the Nanotechnology Conf. and Trade Show (NSTI-Nanotech 2004)*, Boston, MA, USA, 2004;1:355–358.
74. Comtois, J.H. and Bright, V.M., Applications for Surface-micromachined Polysilicon Thermal Actuators and Arrays, *Sens. Actuators A*, 1997;58:19–25.
75. Koester, D.A., Mahadevan, R., and Marcus, K.W., Multi-User MEMS Processes (MUMPS): Introduction and Design Rules, *MCNC MEMS Technology Applications Centre*, Research Triangle Park, NC, *rev. 3*, Oct. 1994.
76. Lin, L. and Chiao, M., Electrothermal Responses of a Lineshape Microstructures, *Sens. Actuators A*, 1996;55:35–41.
77. Huang, Q.A. and Lee, N.K.S., Analysis and Design of Polysilicon Thermal Flexure Actuator, *J. Micromech. Microeng.*, 1999;9:64–70.
78. Thornton, T.J., Pepper, M., Ahmed, H., Andrews, D., and Davies, G.J., One-Dimensional Conduction in the 2D Electron Gas of a GaAs-AlGaAs Heterojunction, *Phys. Rev. Lett.*, 1986;56:1198–1201.
79. Meirav, U., Kastner, M.A., and Wind, S.J., Single-electron Charging and Periodic Conductance Resonances in GaAs Nanostructures, *Phys. Rev. Lett.*, 1990;65:771–774.
80. Liang, C.-T., Simmons, M.Y., Smith, C.G., Kim, G.-H., Ritchie, D.A., and Pepper, M., Coulomb Charging Effects in an Open Quantum Dot Device at Zero Magnetic Field, *Jpn. J. Appl. Phys.*, 2001;40:1936–1940.
81. Smith, C.G., Pepper, M., Ahmed, H., Frost, J.E.F., Hasko, D.G., Peacock, D.C., Ritchie, D.A., and Jones, G.A.C., The Transition from One- to Zero-Dimensional Ballistic Transport, *J. Phys. C: Solid State Phys.*, 1988;21:L893–L898.
82. Liang, C.-T., Simmons, M.Y., Smith, C.G., Kim, G.H., Ritchie, D.A., and Pepper, M., Experimental Evidence for Coulomb Charging Effects in an Open Quantum Dot at Zero Magnetic Field, *Phys. Rev. Lett.*, 1998;81:3507–3510.
83. Smith, C.G., Pepper, M., Ahmed, H., Frost, J.E.F., Hasko, D.G., Newbury, R., Peacock, D.C., Ritchie, D.A., and Jones, G.A.C., Fabry-Perot Interferometry with Electron Waves, *J. Phys. Condens. Matter*, 1989;1:9035–9044.
84. Liang, C.-T., Castleton, I.M., Frost, J.E.F., Barnes, C.H.W., Smith, C.G., Ford, C.J.B., Ritchie, D.A., and Pepper, M., Resonant Transmission Through an open Quantum Dot, *Phys. Rev. B*, 1997;55:6723–6726.